LIMNOLOGY and OCEANOGRAPHY: METHODS

ASLO

Limnol. Oceanogr.: Methods 19, 2021, 589–625

doi: 10.1002/lom3.10447

Hyperspectral optical absorption closure experiment in complex coastal waters

Ina Kostakis,[1,2] **Michael Twardowski**,[3] **Collin Roesler**,[4]* **Rüdiger Röttgers**,[5] **Dariusz Stramski**,[6] **David McKee**,[1] **Alberto Tonizzo**,[3] **Susan Drapeau**[4]

[1]Physics Department, University of Strathclyde, UK
[2]Centre for Healthcare Modelling and Informatics, University of Portsmouth, Portsmouth, UK
[3]Harbor Branch Oceanographic Institute, Florida Atlantic University, Fort Pierce, Florida
[4]Earth and Oceanographic Science Department, Bowdoin College, Brunswick, Maine
[5]Remote Sensing Department, Institute for Coastal Research, Helmholtz-Zentrum Geesthacht, Geesthacht, Germany
[6]Scripps Institution of Oceanography, University of California San Diego, La Jolla, California

Abstract

Accurate measurements of absorption data are required for the development and validation of inversion algorithms for upcoming hyperspectral ocean color imaging sensors, such as the NASA Phytoplankton, Aerosol, Cloud, and ocean Ecosystem mission. This study aims to provide uncertainty estimates associated with leading approaches to measure hyperspectral absorption coefficients in complex coastal waters. Absorption spectra were collected at 12 different stations, all located in the Indian River Lagoon, Florida, USA, between 09 January 2017 and 13 January 2017. Measurements included spectral absorption coefficients in the visible range (400–700 nm) associated with dissolved, a_{CDOM}, total particulate, a_p, and total nonwater, a_{nw}, fractions, and were made both in situ and from discrete samples. Discrete sample approaches included dual-beam spectrophotometer, liquid waveguide capillary cell, point-source integrating cavity absorption meter (PSICAM) for dissolved matter absorption samples, and quantitative filter technique ICAM measurements and the dual-beam spectrophotometer with center-mounted integrating sphere filter pad technique, while the Turner Designs ICAM, and WET Labs AC-s, and AC-9 instruments were used to determine absorption coefficients in situ. The Gershun approach, determining absorption from measurement of the irradiance quartet with respect to depth was also assessed in situ. Measurement uncertainties and relative accuracies were quantified for each of these approaches. Results showed generally strong agreements between different discrete sample methods, with average percent absolute error $\%\delta_{abs} < 7\%$ for a_{CDOM} and $< 9\%$ for a_p. In situ approaches showed higher variability and reduced accuracy. For a_{nw}, $\%\delta_{abs}$ deviation relative to PSICAM data was on average 12% to 20%. Results help identify remaining technological gaps and need for improvements in the different absorption measurement approaches.

Light absorption is a fundamental property of natural waters influencing the propagation of the underwater light field (Mobley 1994; Zaneveld et al. 2005; Woźniak and Dera 2007). Absorption acts as a spectral filter for incident and scattered solar irradiance (e.g., Jerlov 1976; Morel and Prieur 1977; Lewis et al. 1990). Light absorption is commonly quantified as spectral absorption coefficient $a(\lambda)$ (m^{-1}), where λ is the wavelength in vacuum. The accurate quantification of this coefficient and its variability are important for understanding many physical and biological processes in the upper ocean, which are driven by or depend on solar radiation, for example, various photochemical reactions, heating of water column, availability of energy for photosynthesis, or availability of light for animal vision that is important even at mesopelagic depths. Absorption coefficients can provide information on the nature and concentration of various nonwater constituents dissolved and suspended within water (e.g., Twardowski et al. 2005; Woźniak and Dera 2007; Twardowski et al. 2018*a*), such as phytoplankton pigments, taxonomic composition, and size structure of phytoplankton communities (e.g., Organelli et al. 2017). Furthermore, knowledge of absorption coefficients is required to estimate primary production (Behrenfeld and Falkowski 1997).

*Correspondence: croesler@bowdoin.edu

Additional Supporting Information may be found in the online version of this article.

The total absorption coefficient of natural waters, a_t, can be partitioned into the absorption by seawater a_w (m^{-1}), and the absorption by all nonwater components a_{nw} (m^{-1}). The latter can further be divided into the absorption coefficient by colored dissolved organic matter (CDOM), a_{CDOM} (m^{-1}) and the absorption coefficient by particles, a_p (m^{-1}). Coefficient a_p in turn can be separated into absorption by pigmented phytoplankton particles a_{ph} (m^{-1}), and nonalgal particles a_{nap} (m^{-1}). Table 1 summarizes the symbols and abbreviations used in this paper. For detailed definitions of optical properties, see Mobley (1994).

Coupled with the volume scattering function (VSF), absorption can be used to solve the radiative transfer equation for the radiance distribution at depth (disregarding inelastic effects) and is directly related to remote sensing reflectance, irradiance reflectance (E_u/E_d), and diffuse attenuation coefficients that characterize the propagation of light through the water column. Accurate measurements of absorption are also essential for optical models that form the basis of semianalytical inversion algorithms in ocean color remote sensing applications (Werdell et al. 2018). The ability to determine absorption coefficients and associated measurement uncertainties quantitatively is therefore crucial for ocean color algorithm development and validation activities (Tonizzo et al. 2017; IOCCG 2018). Understanding the current state-of-the-art in absorption measurement capabilities and uncertainties, as well as identifying associated gaps, is necessary to prepare for the NASA Plankton, Aerosol, Cloud, and ocean Ecosystem (PACE) mission, which will carry a hyperspectral scanning spectroradiometer and two polarimeters, with launch currently scheduled in 2023 (DelCastillo et al. 2012; Werdell et al. 2019).

Measuring absorption coefficients in a scattering medium that is characteristic of all natural waters is challenging (Tyler 1960) because scattering by suspended material decreases transmitted signals, resulting in systematic overestimation of the true absorption signal using simple beam transmission optics found with common bench top spectrophotometers. A range of absorption meter designs have been developed that attempt to resolve this issue. Reflective tube absorption meters, such as the 25-cm pathlength AC-s (hyperspectral) and AC-9 (multi-spectral) instruments (WET Labs Inc.; www.seabird.com), optimize scattered light collection by using total internal reflection at the outer quartz-air boundary of the wall comprising the sample flow tube to redirect scattered photons toward a diffuser in front of a large area detector (Zaneveld et al. 1992, 1994). These sensors are typically used to measure profiles of in situ total nonwater absorption, a_{nw}, from ships, are integrated in flow-through systems for continuous measurements of surface water (IOCCG Protocol Series—Vol. 2.0, 2019*a*), or are mounted on vehicles towed behind ships (Twardowski et al. 2005). CDOM absorption can be measured on the filtrate passing through a 0.2-μm filter attached to the instrument's intake; a_p is derived by difference. These sensors have been the workhorse for measuring in situ spectral absorption by the oceanographic community since the early 1990s.

Integrating cavity absorption meters (ICAMs) are designed to collect scattered light inside an integrating cavity filled with the water sample (Gray et al. 2006; Musser et al. 2009; Fry 2018). ICAMs can be used to measure absorption either by discrete samples or in flow-through set-ups. Multiple reflections at the cavity walls result in a long effective pathlength and high sensitivity. If a homogeneous, diffuse light field is created inside the cavity, scattering effects become negligible (Fry et al. 1992). Even though their strength is the measurement of a_{nw}, ICAMs can also be used to measure a_{CDOM} when supplied with a filtered sample. The Turner Designs ICAM is an in situ multispectral absorption meter based on this principle and implemented with a backlit cylindrical integrating cavity. Deployment is similar to the in situ reflective tube absorption meters. In point-source ICAMs (PSICAMs), the sample is illuminated with a spherical isotropic light source placed at the center of the integrating sphere (Röttgers 2018). Available instruments include bench-top set-ups following the design by Röttgers et al. (2005) (Sunstone Scientific; www.sunstonesci.com) as well as flow-through versions called OSCAR that can be used for in situ deployments and inline systems (TriOS; www.trios.de). Because of the negligible effect of scattering and the rigorous characterization of uncertainties with the PSICAM across a broad spectral range, this approach is currently considered the state-of-the-art (IOCCG Protocol Series—Vol. 5.0, 2020).

Another, although rarely used, in situ method uses Gershun's (1939) equation to calculate the total absorption coefficient from measurements of the irradiance quartet, or equivalently from measurements of the net planar irradiance and total scalar irradiance. The irradiance quartet includes the downwelling and upwelling planar irradiances, E_d and E_u, as well as downwelling and upwelling scalar irradiances, E_{od} and E_{ou}, which are used to compute net irradiance, $E = E_d - E_u$, and total scalar irradiance, $E_o = E_{od} + E_{ou}$. Few experimental studies have incorporated simultaneous measurements of both spectral plane and scalar irradiances (Tyler et al. 1958; Tyler 1960; Pegau et al. 1995), and we are aware of only a single recent study providing an explicit presentation of experimental data of the full irradiance quartet with high spectral resolution (Li et al. 2018). In contrast to other absorption techniques, the Gershun approach of determining absorption coefficient relies on the measurement of the natural light field in aquatic environments, so it does not use an artificial light source and has the advantage that sample volumes are large, that is, more consistent with above water determinations of ocean color reflectance (Mobley 1999). In addition, the water is virtually unperturbed by the measurement because the method does not rely on pumps or discrete water sampling. A limitation is that the measurements are limited to the depth of the euphotic zone and to daylight hours with high solar elevation.

Other laboratory techniques have been optimized to measure specific partial absorption coefficients accurately. This

Table 1. List of symbols and abbreviations.

Symbol	Meaning	Units
a_t	Total absorption coefficient	m^{-1}
a_w	Absorption coefficient by seawater	m^{-1}
a_{nw}	Absorption coefficient by all nonwater components	m^{-1}
a_p	Absorption coefficient by particles*	m^{-1}
a_{CDOM}	Absorption coefficient by colored dissolved organic matter*	m^{-1}
a_{ph}	Absorption coefficient by pigmented phytoplankton particles	m^{-1}
a_{nap}	Absorption coefficient by nonalgal particles*	m^{-1}
c_t	Total attenuation coefficient†	m^{-1}
c_{nw}	Attenuation coefficient by all nonwater components†	m^{-1}
Chl *a*	Chlorophyll *a* concentration	Mg m^{-3}
$\%\delta_{abs}$	Mean absolute percentage error	%
$\%\delta_{rel}$	Mean relative percentage error	%
E	Net irradiance	Wm^{-2}
E_d	Downwelling planar irradiance	Wm^{-2}
E_u	Upwelling planar irradiance	Wm^{-2}
E_{od}	Downwelling scalar irradiance	Wm^{-2}
E_{ou}	Upwelling scalar irradiance	Wm^{-2}
λ	Wavelength	Nm
n	Number of samples/measurements	—
OD	Optical density	Dimensionless
POC	Particulate organic carbon concentration*	mg m^{-3}
q	(Sample) observation (i.e., absorption measurement)	—
q_{ref}	Reference observation	—
$\overline{q}$	Arithmetic mean of absorption parameter measured	—
ρ	Constants for ISFP a_p calculation, $\rho = 2.303 \times 100 \times 0.323$	
$s()$	Standard deviation	—
SPM	Suspended particulate matter concentration*	g m^{-3}
u_c	Combined uncertainty	—
u_{nat}	Experimental uncertainty associated with natural variability	—
u_o	Operational uncertainty not including natural variability	—
z	Water depth	m
Abbreviations		
CDOM	Colored dissolved organic matter	
CI	Confidence intervals	
HCl	Hydrochloric acid	
H_2O_2	Hydrogen peroxide	
ICAM	Integrating cavity absorption meter	
ISFP	Integrating sphere filter pad method	
LWCC	Liquid waveguide capillary cell	
NASA	National Aeronautics and Space Administration	
NaOCl	Sodium hypochlorite	
NIR	Near-infrared	
PACE	Phytoplankton, Aerosols, Cloud, and ocean Ecosystem mission	
PSICAM	Point-source integrating cavity absorption meter	
QFT-ICAM	Quantitative filter technique integrating cavity absorption meter	
RMSD	Root mean square deviation	
%RMSD	Percent root mean square deviation	
UV	Ultraviolet	
VSF	Volume scattering function	

*Operationally defined by filter pore size.
†Operationally defined by some acceptance angle in collimated detector optics.

includes the measurement of a_{CDOM} from discrete samples. Traditionally, a_{CDOM} has been measured in a dual-beam spectrophotometer equipped with glass cuvettes relative to pure water (Bricaud et al. 1981) and more recently of sample passed through syringe filters into an UltraPath or liquid waveguide capillary cell (LWCC, both World Precision Instruments Inc.) system (IOCCG Protocol Series—Vol. 5.0, 2020). Determination of a_{CDOM} is typically less problematic because the amount of scattering has been reduced to a negligible level by filtration. Some scattering materials, such as small particulate matter, colloids, and (micro-) bubbles, however, potentially remain in the sample after filtration, which may result in measurement uncertainties of unknown magnitude (Stramski and Woźniak 2005; Zhang and Gray 2015, 2020). However, measurements of a_{CDOM} in both absorption and attenuation flow cells of AC devices have generally shown excellent agreement, that is, within respective uncertainties, in extensive measurements across a broad range of natural waters, indicating effects of scattering by colloids may be considered negligible (Twardowski et al. 2004). Measurements of a_{CDOM} in standard bench-top spectrophotometers, such as single-beam or dual-beam spectrophotometers, can also suffer from relatively low sensitivity due to a maximal geometric pathlength associated with 10-cm cuvettes.

Measurements with a LWCC are fast, use very small sample volumes (a few mL), and have the advantage of sensitivity due to long optical pathlengths (up to 2 m^{-1}). LWCC measurement uncertainties are generally better than 0.01 m^{-1} or 5% to 10% accuracy depending on wavelength, with highest relative uncertainties at longer wavelengths where the absorption signals are low (IOCCG Protocol Series—Vol. 5.0, 2020). These absorption measurements are, however, extremely susceptible to the presence of bubbles in the system. Other sources of uncertainty include issues with pathlength accuracy, salinity (i.e., refractive index) dependencies, light source stability, and detector issues such as internal scattering errors, nonlinearity, and wavelength inaccuracies, similar to other techniques using broad spectral illumination (Lefering 2012). Potential effects of scattering by very small particles in the colloidal/nanoparticle size range may also be a concern in some cases (Röttgers et al. 2005; Floge et al. 2009; Lefering et al. 2017).

The quantitative filter pad technique measures particulate absorption a_p for particles collected on glass fiber filter pads through filtration. Different filter pad approaches have been developed over the years (e.g., Yentsch, 1962; Mitchell and Kiefer 1998; Tassan and Ferrari 1995), with most accurate setups, that is, the bench top spectrophotometric integrating sphere filter pad (ISFP) method (Maske and Haardt 1987; Röttgers and Gehnke 2012; Stramski et al. 2015; Roesler et al. 2018) and the quantitative filter technique ICAM (QFT-ICAM; Röttgers et al. 2016), measuring absorption from filter pads placed inside an integrating sphere to reduce measurement artifacts introduced by scattering by the filter.

In this study, we provide a generational sequel to the comparative work of Pegau et al. (1995) by comparing a wider range of state-of-the-art methods and improved techniques to measure spectral absorption coefficients of natural waters including dissolved, particulate, and nonwater fractions, both in situ and from discrete samples. We report and compare only absorption data in the visible range of the spectrum (400–700 nm), as this range is common to all compared techniques and is most relevant to ocean color applications although sensors for the PACE mission will also extend into the ultraviolet (UV), at least to 350 nm. Measurement uncertainties and accuracy are quantified for each of the state-of-the-art approaches. Results provide uncertainty estimates associated with hyperspectral absorption data, which are required for the validation and development of inversion algorithms for upcoming hyperspectral ocean color imaging sensors aboard the PACE mission. A key objective of this exercise is assessing relative accuracies for very different approaches, each with their own sources of uncertainty ranging from well characterized to perhaps unknown at this time, to give us the best possible estimate of how close we may approximate true absorption.

Material and methods

Absorption spectra were measured at 12 different stations, all located in the Indian River Lagoon along the central Atlantic coast of Florida, USA, between 09 January 2017 and 13 January 2017 (Fig. 1). All stations were well-mixed, shallow (bottom depth < 4 m) and relatively turbid with nonwater attenuation c_{nw} at 532 nm ranging between about 1.5 and 10 m^{-1}. Data and samples were collected at a single depth only, about 1–2 m from the surface, with the exception of the Gershun method, for which irradiance measurements at multiple depths are required (for more details, see below). In situ measurements were collected over long intervals (approx. 30 min) to quantify any natural variations across instruments and samples. Water samples were collected at the depth of in situ absorption observations using Niskin bottles. On board, water from multiple Niskin bottles was transferred to a single 20-L carboy which was gently mixed and rapidly subsampled to ensure uniformity. Table 2 shows a list of absorption parameters measured with different techniques.

Discrete sampling approaches

Ancillary characterization of particulate matter

The mass concentrations of suspended particulate matter (SPM), particulate organic carbon (POC), and chlorophyll *a* (Chl *a*) were determined following collection of particulate matter by filtration onto 25-mm Whatman glass fiber filters (GF/F). The volume of water filtered for these determinations varied from 200 to 500 mL. SPM (g m^{-3}) was measured using a standard gravimetric technique (van der Linde 1998).

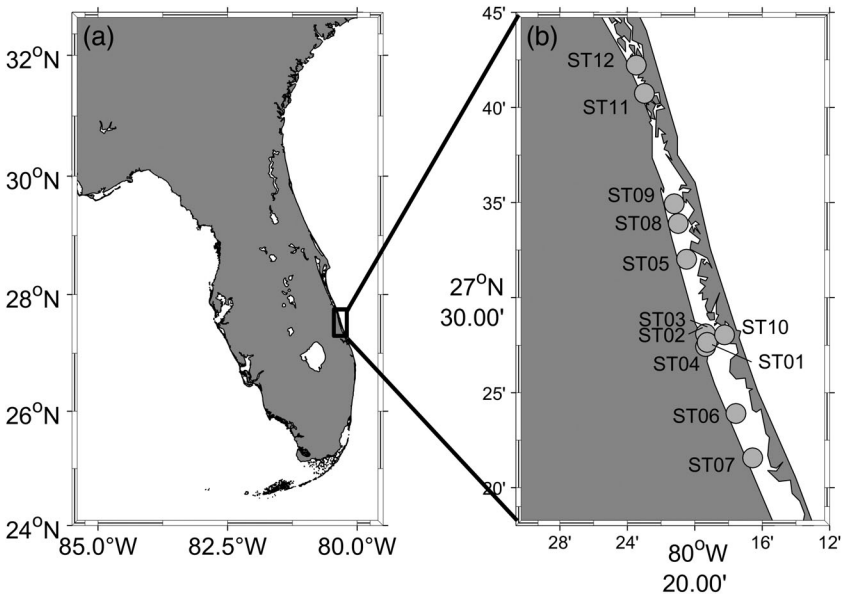

Fig 1. Maps of (**a**) Florida, USA and the sampling area, and (**b**) sampling locations in the Indian River Lagoon.

Particles were collected on prerinsed, precombusted 25-mm GF/F filters that were weighed prior to use. Following filtration under low vacuum (≤ 120 mmHg), sample filters and edges were rinsed with deionized water to remove residual sea salt, dried at 60°C, and stored sealed until postcruise analysis in the laboratory. The mass of particles collected on the filters was determined with a Mettler-Toledo MT5 microbalance with 1-μg precision. POC (mg m^{-3}) was obtained using a method consistent with established protocols (Parsons et al. 1985; Knap et al. 1994). Water samples were filtered through precombusted 25-mm GF/F filters, filters were transferred to clean glass scintillation vials and dried at 60°C, then stored until postcruise analysis. Prior to analysis, filters were exposed to concentrated acid fumes (HCl) to remove inorganic carbon. Then, the organic carbon content of each filter was determined with standard carbon, hydrogen, and nitrogen analysis involving high-temperature combustion of sample filters. A number of unused filters from each lot of precombusted filters were used to quantify the background carbon content of filters and subtracted from the sample data. These blank filters were treated exactly like sample filters except that no sample water was passed through them. Sample filtration volumes were large enough to ensure that contributions of the blank filter or adsorbed dissolved organic carbon were small relative to the particulate carbon content on sample filters. For both the SPM and POC, duplicate samples were typically taken for each station and averaged to produce the final results. The duplicates for SPM and POC agreed well with the coefficient of variation generally less than about 5% for SPM and less than 10% for POC. For Chl *a* determinations the samples collected on GF/F filters (filtration volume varied between 200 and 400 mL) were flash frozen and stored and shipped in liquid nitrogen until postcruise analysis. Chl *a* (mg m^{-3}) was determined by high-performance liquid chromatography by the Ocean Ecology Laboratory at NASA Goddard (Van Heukelem and Thomas 2005). Replicates were taken at 3 of the 12 stations.

In addition to information about particle concentration, the measurements of SPM, POC, and Chl *a* provide useful proxies of bulk composition of particulate matter. Specifically, the organic vs. inorganic fractions of SPM can be characterized using the ratio POC/SPM, and the contribution of phytoplankton to SPM using Chl *a*/SPM. These ratios are expressed on a (g/g) basis.

PSICAM method

The PSICAM was used to measure a_{nw} and a_{CDOM}, following the set-up, calibration and protocol described in Röttgers et al. (2005, 2007, and 2018) and Lefering et al. (2018). The set up uses a broad band light source coupled to an optical fiber that delivers light to the diffuse point source in the middle of a 9-cm diameter spectralon cavity. A spectrometer (AvaSpec ULS2048XL, Avantes) disperses light on the detection side. The system was calibrated using a Nigrosine (Certistain, Merck) solution, with the absolute spectral absorption coefficient of this solution measured with a LWCC (see below). Calibration is used to determine the reflectivity of the cavity. Prior to each calibration the PSICAM cavity was bleached with a weak sodium hypochlorite solution for 10 min and then rinsed thoroughly. The temperature of Nigrosine solution and purified water were recorded for temperature correction during subsequent data processing. Calibrations with Nigrosine were performed daily, with at least three replicates spread out over the course of a day in order to

Table 2. Summary of different absorption parameters measured with different absorption techniques. For ICAM, AC-9, and the ISFP method, two data sets were collected with independent instrument systems. In this study, only absorption data in the visible range (400–700 nm) was reported, compared and assessed.

Instrument	Method	Number of sensor systems	Original spectral range (resolution)	Absorption parameter(s) directly measured	Absorption parameter derived
PSICAM	Bench top integrating sphere	1	360–728 nm (2 nm)	a_{nw}, a_{CDOM}	a_p
Turner Designs ICAM	In situ integrating cavity	2	365, 440, 488, 510, 532, 555, 590, 630, 676	a_{nw}, a_{CDOM}	a_p
WET Labs AC-s	In situ reflective tube	1	AC-s 1: 399–741 nm (mean: 4 nm) AC-s 2: 401–726 (mean: 3.7 nm)	a_{nw}	—
WET Labs AC-9	In situ reflective tube	2	412, 440, 488, 510, 532, 555, 650, 676, 715	a_{nw}	—
TriOS irradiance quartet	Gershun	1	320–900 nm (2 nm)	a_t	a_{nw}
ISFP	Bench top spectrophotometer with filter pad inside integrating sphere	2	ISFP 1: 400–750 nm ISFP 2: 300–850 nm (both 1 nm)	a_p, a_{nap}	a_{ph}
QFT-ICAM Filter pad	Bench top integrating sphere with filter pad inside cavity	1	340–844 nm (2 nm)	a_p, a_{nap}	a_{ph}
LWCC	Bench top capillary waveguide	1	240–750 nm (2 nm)	a_{CDOM}	—
Cary E3 UV–VIS spectrophotometer	Bench top dual-beam spectrophotometer with 10-cm cuvettes	1	400–750 nm (1 nm)	a_{CDOM}	—

monitor potential changes in the cavity's reflectivity. Parameter a_{nw} was determined from untreated samples in triplicate against purified water as reference, alternating reference and the sample. Measurements were corrected for temperature and salinity effects and chlorophyll fluorescence effects. For the latter, additional measurements of the light intensity inside the cavity were made with illumination restricted to wavelengths < 620 nm with a short pass interference filter. For a_{CDOM} measurements, samples were filtered through a 0.22-μm pore size membrane filter (GSWP, Merck Millipore Ltd, Cork, Ireland), using low vacuum < 0.2 bar. Absorption was measured in triplicate, following the same protocol (without fluorescence correction). PSICAM a_p was determined by subtracting a_{CDOM} from a_{nw} spectra. The PSICAM has recently become available commercially.

As in all other methods, a series of corrections is applied to PSICAM observations to derive final absorption coefficients. The PSICAM, however, offers the powerful advantage that measurements are negligibly affected by particle scattering. Reported measurement uncertainties for PSICAM data are on average 0.006 m^{-1} (8%) for a_{nw} and 0.002 m^{-1} (13%) in the case of a_{CDOM}, varying with wavelength. This reflects a combination of underlying wavelength dependencies in lamp output, wall reflectivity, detector sensitivity, and sample absorption (Lefering et al. 2018). Measurement uncertainties increase toward the extremities of the visible spectrum where they can well exceed these average levels. This can result in limitations in accuracy of PSICAM data at blue wavelengths in highly turbid waters (Lefering et al. 2016).

Artifacts due to stray light effects inside the detector were corrected by subtracting the detected raw intensity signal measured at wavelengths outside the lamp emission range (180 nm) as a flat offset across the spectrum before conversion into absorption spectra (detailed description in Lefering et al. 2017). Nonlinearity was corrected using nonlinearity correction factors available for the individual Avantes sensors. Wavelength accuracy of the detectors was checked and, when necessary, corrected using an Avantes AvaLight Cal-Mini spectral calibration light source, accuracy ± 0.3 nm.

ISFP method

Three different labs measured particulate absorption with the filter pad technique. Two groups of investigators measured a_p and a_{nap} with the ISFP method in the laboratory after the

cruise; these results are designated ISFP 1 and ISFP 2 and the relevant methodology is described in this section. The third group measured a_p on board the ship using the QFT-ICAM technique shortly after collecting the samples, which is described below.

For each discrete water sample three sets of three replicate sample filters (GF/F, 25-mm Whatman glass-fiber filters) were prepared using the same filtration rig by the same operator, to ensure minimal bias across sample filters. These sets of replicate filters were then used by the three groups of investigators. Filtration volumes varied between 100 and 300 mL, which ensured that the measured optical density (OD) corresponding to particulate absorption on the filters was kept within desired range of values below 0.4 in the visible spectral region. For the ISFP method, sample filters were flash-frozen, stored, and shipped in liquid nitrogen, and measured in the lab postcruise. Reference (blank) filters for each station were prepared by filtering the same volume of freshly filtered sea water through a clean GF/F filter and also stored in liquid nitrogen for postcruise measurements of reference filters. The average diameter of the filter clearance area for the filtration rig and filter operator was measured prior to the cruise, using filters with high particulate load and digital calipers (accuracy $\pm$ 0.001 mm, resolution 0.01 mm). The average diameter of the filter clearance area for the filter rig across the set of six filter cups was 22.30 mm ($\pm$ 0.8 mm). The volume filtered was determined with 100- and 250-mL Nalgene graduated cylinders (resolution 0.5 and 1.0 mL resolution, respectively). Precise volume was obtained using a glass pipette to add/remove volume to the measurement line.

The ISFP method involves the measurement of sample and blank filters placed inside the integrating sphere of a spectrophotometer and is described in detail elsewhere (Röttgers and Gehnke 2012; Stramski et al. 2015; Roesler et al. 2018). This measurement geometry efficiently reduces the uncertainty associated with light scattering to a very small or negligible level. ISFP 1 and ISFP 2 data were collected with dual-beam spectrophotometers (Cary 300, Agilent, Inc. and Lambda 18, Perkin-Elmer, Inc., respectively) each equipped with the same model 15-cm integrating sphere (RSA-PE-18, Labsphere, Inc.). These data were acquired in the spectral region from 350 to 780 nm (ISFP 1) and 300 to 850 nm (ISFP 2), using a 2-nm slit and a 1-nm interval. In this study, only the data from the visible range (400–700 nm) are reported. For every sample filter, the spectral scans of OD of particulate matter on the filter were measured for two different orientations of the filter. These scans showed excellent reproducibility and were averaged. For each station, the measurements were made on three replicate sample filters. Typically, the reproducibility between these three replicates in terms of derived values of a_p was very good with a coefficient of variation remaining below 2% or 3% across the visible spectral range. The final results represent the average values based on these three replicates. For a few stations (i.e., ST02, ST07, and ST09); however, the final absorption results in the ISFP 2 data set are based on averaging measurements taken on duplicate sample filters. In these cases, the rejected measurement on the third replicate filter was considered an outlier as it would increase the coefficient of variation to about 8–10% across the spectrum. Such "outlying" measurements (albeit still in relatively good agreement with other replicates) were associated with uneven distribution of particles on filters, which was clearly visible as a "bubbling up" on the rejected replicate filters. In the ISFP 1 data set all three replicates for a given sample were averaged to derive the final sample spectrum, and this was done for all stations.

The derivation of spectral values of a_p from the ISFP method requires the correction of sample measurements for the OD of reference (blank) filters. In our experiments the reference spectrum was determined by averaging the measurements taken on several blank filters (five and six blank filters, respectively, for the ISFP 1 and ISFP 2 data sets). In addition, the intrinsic instrument baseline of the spectrophotometers was monitored throughout the period of sample measurements to account for instrument noise or potential temporal drift of instrument baseline. This instrument baseline was measured with empty optical path in both sample and reference beams (i.e., the spectral scan of air vs. air). For the spectrophotometers used in our study this noise is always very small compared to the measured absorption signal (except when the signal is nearly null, e.g., the particle absorption in the infrared spectral region). The potential drift over a period of several hours when sample measurements are taken was also either very small or undetectable. Nevertheless, the optical densities of sample and blank filters were corrected for this instrument baseline. Finally, the sample optical densities (after correction for instrument baseline and reference filter) were corrected for pathlength amplification using the equation for the ISFP method from Stramski et al. (2015) and then converted to the spectral values of a_p using the clearance area of the filter and volume of filtered sample.

Upon completion of spectral scans for the determination of a_p, the sample filters were immediately subject to methanol treatment with a purpose of extracting pigments that are associated mostly with phytoplankton (Kishino et al. 1985; Roesler et al. 2018) to derive the absorption of particulate matter remaining on the filter after extraction, that is, nonalgal particulate absorption, a_{nap}. The spectrophotometric measurements of filters after methanol extraction and calculations of a_{nap} were done in a similar way as described for a_p. We note that the difference between the measurements of a_p and a_{nap} represents absorption by the methanol-extractable pigments in vivo, that is, packaged as they were in the cell, and thus approximating the phytoplankton absorption coefficient, a_{ph}. We note that phycobilipigments are not methanol extractable, additional treatments with phosphate buffer are required to remove these pigments from the filter when present in

nonnegligible concentrations. This additional extraction was not necessary for these samples.

Estimates for uncertainties in ISFP measurements can be determined by arithmetically propagating uncertainties for each methodological step (Roesler et al. 2018). The resulting aggregated uncertainty includes errors from measured OD, pathlength amplification correction, filtered volume, filter clearance area, as well as additional sources of uncertainties associated with sample type, particle characteristics, sample handling, and storage. Rigorous quantification of total uncertainty of filter pad method is difficult because information required to rigorously evaluate the effects associated with all sources of error are generally unavailable. Most sources of uncertainties can, however, be minimized through careful experimental practice (e.g., accurate measurements of filtered volume and filter clearance area) and replicate measurements of OD (e.g., replicate sample filters and replicate spectral scans of the same filter) and such practice was followed in this study. A correction for pathlength amplification has been identified as one of the most important sources of error, especially because this correction depends not only on particulate load on the filter but also, to some extent, on the composition of particulate assemblage (Bricaud and Stramski 1990; Röttgers and Gehnke 2012; Stramski et al. 2015; Lefering et al. 2016). Röttgers and Gehnke (2012) determined an median error of < 14% for a large number of measurements of algal cultures and natural samples, while the study by Stramski et al. (2015) of diverse samples characterized by a wide range of particulate composition determined a median error associated with variability in pathlength amplification of about 7% for ISFP measurements of a_p.

QFT-ICAM method

A third group of investigators used the QFT-ICAM approach (Röttgers et al. 2016) to measure a_p on filters on board the vessel within minutes of filtration. This approach measured absorption coefficients from 340 to 844 nm. Filters were prepared by the same method and operator as for ISFP measurements (see above) but particle concentration for the QFT-ICAM filters was lower (OD < 0.2) than for ISFP filters following the recommendations given in Röttgers and Gehnke (2012). Each filter was measured three times in random orientations, with a reference measurement before and after each sample measurement. Measurements were corrected for Chl *a* fluorescence effect using additional measurements when wavelengths of fluorescence, that is, at > 620 nm, are excluded from the illumination. Data were also corrected for pathlength amplification using the method of Stramski et al. (2015) to allow direct comparison with the other ISFP measurements without bias from different pathlength corrections. For pigment removal, filters were bleached with NaOCl (Ferrari and Tassan 1999), which was removed after a few minutes with a few drops of H_2O_2. Bleached filters were measured once approximately 30 min after H_2O_2 treatment. We note that bleach treatment does not remove pigments from the sample as is done with methanol extraction, but oxidizes the molecules, thereby shifting absorption into the UV. The advantage of this treatment is that the nonmethanol extractable phycobilipigments are oxidized. In addition to uncertainties associated with preparation of the filter paper, such as inhomogeneity, other sources of error are potential issues with the detector (wavelength calibration, sensitivity, internal stray light, nonlinearity), fluorescence by pigments other than Chl *a* and uncertainties in the pathlength amplification correction. Measurements were corrected for nonlinearity, wavelength inaccuracy, and internal stray light of the detector using the same methodology as described above (see above).

LWCC method

CDOM absorption a_{CDOM} was measured using a LWCC system (World Precision Instruments Inc.), with a 0.5-m pathlength and a 2-m pathlength (*see* Lefering et al. 2017, for details on the set-up, components, and methods). Samples were filtered through 0.2-μm pore-sized Spartan size syringe filters (Whatman) while being injected into the capillary cell using a peristaltic pump. Absorption coefficients were measured from 240 to 500 nm with the 50-cm pathlength cell and from 300 to 750 with the 200-cm pathlength at 2-nm resolution (raw intensity spectra were binned from 0.3 to 2 nm prior to absorption calculation). Measurements were made in triplicate against purified water (Milli-Q) and averaged spectra were subsequently corrected for salinity and temperature effects on the absorption by pure water, as well as for nonlinearity, wavelength inaccuracy, and internal stray light of the detector using the same methodology as described above. Next, the two absorption spectra were compared within the range of overlap, 300–500 nm. Spectra were found to be in good agreement and combined to a single spectrum using data from the short pathlength LWCC between 240 and 350 nm, and data from the long pathlength LWCC at > 350 nm. All LWCC absorption data used for comparison in this study were measured with the longer pathlength but quality controlled using data from the independent shorter pathlength system. Merged absorption spectra were then smoothed using a five-point moving average and offset corrected at 700 nm (Fig. 2). Offset correction was only applied to remove small offsets below the detection limit, assuming that the absorption was approximately zero at 700 nm and the residual errors are spectrally independent. The latter is not known and the assumption might not hold true, however, any error introduced by offset correction was shown to be negligible.

Implementation of the state-of-the-art CDOM measurement protocols should limit measurement uncertainties to within 0.01 m^{-1} (IOCCG Protocol Series—Vol. 5.0, 2020). Cross-comparison between different LWCC set-ups and the PSICAM have shown LWCC uncertainties well within this range with root mean square deviation (RMSD) of 0.007 m^{-1}

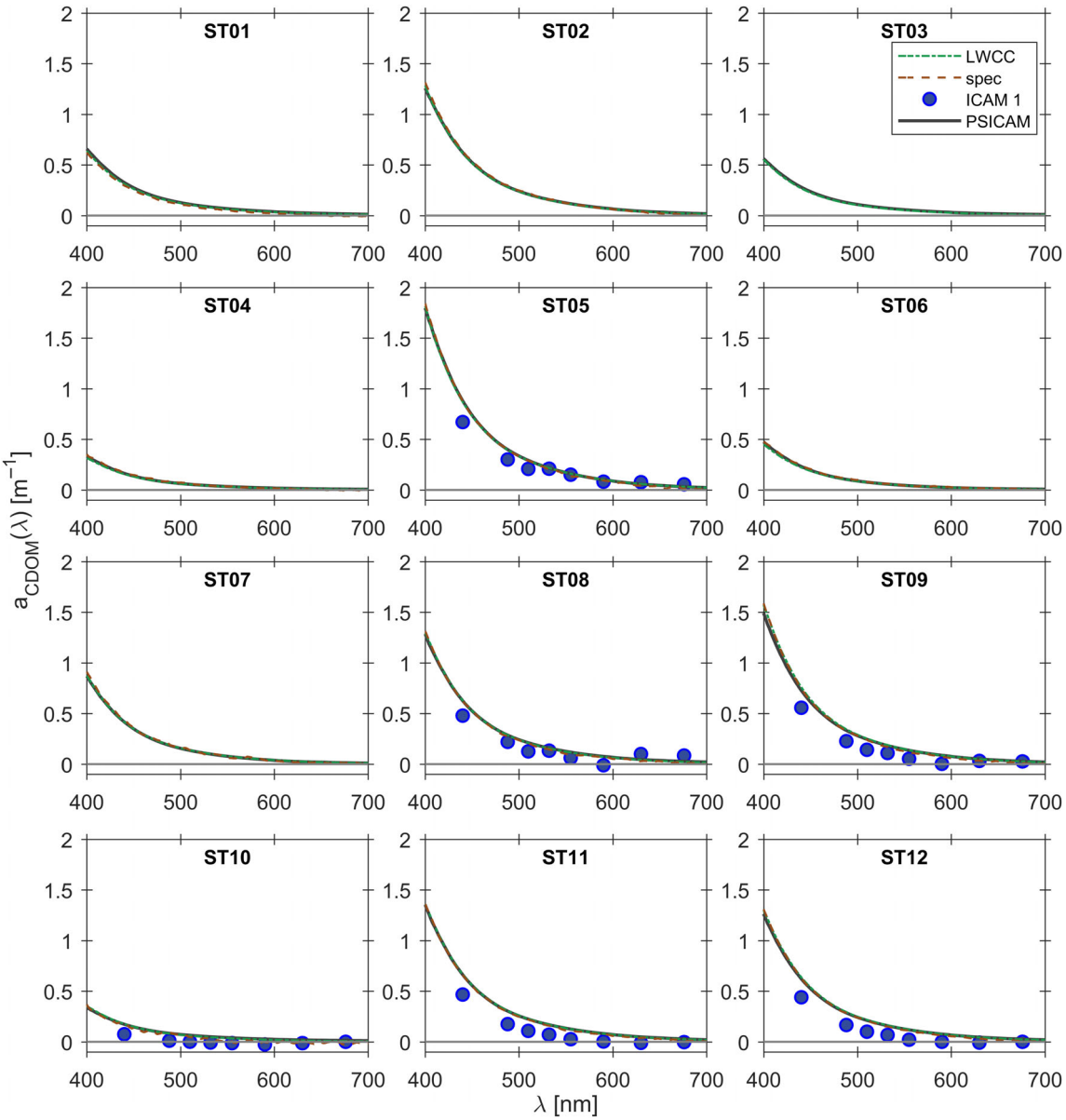

Fig 2. CDOM absorption spectra, a_{CDOM}, measured with LWCC, dual-beam spectrophotometer, ICAM 1, and PSICAM for all stations.

at 440 nm. Uncertainties are wavelength dependent, reflecting underlying wavelength dependencies in lamp output, sensor sensitivity, internal detector stray light, effect of salinity and temperature corrections, and CDOM absorption characteristics (Lefering et al. 2017).

Dual-beam spectrophotometer method

Filtrate from the particulate absorption filter pads was collected in Amber glass bottles after triplicate rinses with the sample. The sample bottles were stored and shipped frozen for analysis in the laboratory. The absorption by the dissolved fraction was measured spectrophotometrically in a Cary 300 configured in a dual-beam transmission mode. Samples were measured in 10-cm quartz cuvettes using Milli-Q© water as the reference material. All samples were measured in a single session; the temperature of the sample and reference materials was maintained by storing the sample and reference bottles in a tub of room temperature water. The absorption coefficients were computed from the OD scans, converting from $\log_{10}$ to $\log_e$ (absorbance to absorptance), and scaling to the geometric pathlength of the cuvette in meters. The scans were corrected for differences in temperature and salinity between the sample and the reference material following Sullivan et al. (2006).

Table 3. Summary of scattering correction methods for AC devices tested in this work.

Method	Description	Scattering error, $\varepsilon(\lambda)$
Flat (or baseline)	Constant spectral subtraction of measured absorption at reference wavelength in the NIR (Zaneveld et al. 1994)	$a_m(\lambda_{ref})$
Proportional	Spectral subtraction of absorption at reference wavelength in NIR scaled spectrally to estimated total scattering (Zaneveld et al. 1994)	$a_m(715)\left(\frac{c_m(\lambda)-a_m(\lambda)}{c_m(715)-a_m(715)}\right)$
Semiempirical	Constant spectral subtraction of empirical estimate of absorption error at reference wavelength in NIR (*see* Röttgers et al. 2013)	$a_m(715)-0.212a_m(715)^{1.135}$
VSF based	Constant spectral subtraction of independent estimate of ε from VSF measurements β and modeled angular weighting function W with 98% reflectivity for reflective tube from McKee et al. (2013) (*see* Stockley et al. 2017)	$2\pi\int_0^{\pi}\sin(\theta)\beta(\theta,658)W(\theta)\,d\theta$

In situ approaches

WET Labs AC-s and AC-9

Two 25-cm flow cell AC-9 and two 25-cm flow cell AC-s devices were integrated on a profiling package with a SBE-49 conductivity temperature depth sensor (CTD). The package also included the Multiangle Scattering Optical Tool to measure the VSF between 10° and 170° in 10° increments (Sullivan et al. 2006; Twardowski et al. 2012). Data from VSF measurements were used in one of the corrections for scattering in the absorption measurement from the AC devices (Table 3). AC devices were mounted vertically and plumbed following Twardowski et al. (1999), which included degassing Y's to enable air evacuation when submerged. The second AC-s did not consistently degas in these very shallow waters, however, so the data are not considered here. After measurements in whole seawater, a 0.2-μm prefilter (Pall Maxi-capsule) was fitted to the AC-s to measure a_{CDOM}. Degassing was more difficult with the prefilter restricting flow, and all a_{CDOM} data were disregarded due to concerns over persistent bubbles contaminating measurements in these shallow, warm waters. Optical windows and flow cells were cleaned with a 50% ethanol solution daily before field measurements. Purified water calibrations were carried out daily before and after field measurements in the configuration they were deployed (Twardowski et al. 1999). Time series for all measurements were collected at 1–2 m depth at each station.

Postprocessing of AC absorption data included application of calibration water blanks and correction for temperature and salinity effects on pure water absorption using coefficients from Twardowski et al. (1999) and Sullivan et al. (2006). Subsequent scattering corrections applied to these processed absorption coefficients a_m are listed in Table 3, where $a_{nw}(\lambda) = a_m(\lambda) - \varepsilon(\lambda)$, with ε being the scattering error; ε accounts for light that was not absorbed but did not reach the diffuser at the end of the flow tube. On a relative basis ε is very significant, often more than half of a_m, especially in the red. The iterative scattering correction (McKee et al. 2013) was not included in this comparison due to a lack of spectrally resolved backscattering data. Corrected absorption spectra were interpolated linearly to 2-nm resolution in the visible range.

Operational uncertainties for AC absorption spectra vary from sensor to sensor but typically are estimated to be 0.005–0.01 m^{-1} for absorption magnitudes up to several 1 m^{-1}, not taking into account errors associated with the scattering correction (Twardowski et al. 2018*b*). At absorption values greater than about 20 m^{-1}, uncertainties increase dramatically. AC-s devices typically have higher uncertainties than AC-9 devices, particularly in the short visible range due to differences in lamp and detector stability and higher spectral dispersion reducing incident intensity for each band. Also, within the instrument, the AC-s automatically applies filter factors to the measured absorption spectrum to smooth the effects of the integrated linear variable filters with step ranges of 14–18 nm (Sullivan et al. 2006). AC-s absorption spectra therefore need to be "unsmoothed" to retrieve the actual measured absorption spectrum (Zaneveld et al. 2004; Chase et al. 2013).

ICAM method

Multispectral absorption was estimated from two Turner ICAM sensors, which were mounted on a dedicated optical profiling package. Absorption was measured at nine wavelengths determined by the nominal peak of the nine source LEDs: 365, 440, 488, 510, 532, 555, 590, 630, and 676 nm, with the LED FWHM varying from 10 to 30 nm depending upon source wavelength. Data were collected over several minutes, and medians and standard deviations were calculated. As with AC-s and AC-9 measurements, pure water calibrations were collected daily on board. The spectral mean values of the water calibration varied from −0.063 m^{-1} at 365 nm to 0.035 m^{-1} at 676 nm, increasing spectrally from blue to red. Standard deviation of daily water calibrations were of order 0.010–0.039 m^{-1} from blue to red. The average water

calibration spectrum was applied to the station mean unfiltered and filtered absorption spectra. Measurements were then corrected for wavelength-specific temperature and salinity effects following Sullivan et al. (2006). These corrections were $< 10^{-3}$ m^{-1} at all wavelengths with the exception of 590 nm where the correction was approximately 0.005 m^{-1}.

Gershun method

Absorption spectra were calculated from hyperspectral measurements of the irradiance quartet, E_d, E_u, E_{od}, E_{ou}, using Gershun's law (Gershun 1939; Højerslev 1975). The profiling package, consisting of four RAMSES sensors (Trios GmbH), was lowered to specific depths to collect data over a 2-min period at each depth (2–9 depths per station). The radiometry package was positioned so that ship shadow effects were minimal.

Spectra were linearly interpolated from 3.2- to 2-nm intervals from 320 to 900 nm. Both conversion of sensor pixel to corresponding wavelengths and correction for immersion effects were calculated for each sensor with the coefficients provided by the manufacturer. Data were processed broadly following Li et al. (2018), where noise was removed using a Savitzky–Golay filter, wavelengths were interpolated, and measurements with signal below the detection limit of 10^{-6} W m^{-2} nm^{-1} were removed from the analysis. All underwater radiometry profiles were corrected for changes in the incident solar radiation, measured concurrently with a deck reference sensor (also TriOS RAMSES) measuring downwelling above surface irradiance, E_s, during a cast sequence. Individual radiometry profiles were composed during postprocessing, using median values of each radiometric parameter at each depth step. Unfortunately, we were unable to mount all radiometers so that upwelling and downwelling collectors and the depth sensor aligned in the same horizontal plane, with offsets varying between 8 and 18 cm. During the last step prior to calculation of absorption coefficients, radiometry profiles were therefore interpolated to the same depth.

Absorption was calculated solving Gershun's equation Eq. 1, which is derived from the radiative transfer equation for radiance, ignoring inelastic radiative processes in the water column (Jerlov 1976; Mobley 1994):

$$\frac{d}{dz}(E_d - E_u) = -a_t E_o, \tag{1}$$

where E_d and E_u are planar downwelling and upwelling irradiance, respectively. Total scalar irradiance E_o is the sum of E_{od} and E_{ou}, the scalar downwelling and upwelling irradiance, respectively. The approach is, therefore, not expected to work for situations when inelastic processes have significant effect on underwater light fields, especially in the long-wavelength portion of the visible spectrum where Raman scattering by water molecules or Chl *a* fluorescence can have a significant effect, depending on water optical properties.

The term on the left site of the equation was derived by fitting a linear regression model to the log-transformed (E_d – E_u) vs. depth with subsequent transformation back into linear space. All depths were included in the regression, assuming exponential decrease in (E_d – E_u) with depth at all wavelengths, which was found to be an accurate approximation in these shallow waters. Equation 1 was then evaluated at each depth where measurements were available. Literature values for the absorption by seawater (Pope and Fry 1997) corrected for temperature and salinity effects (Sullivan et al. 2006) were subtracted to derive a_{nw} for comparison with PSICAM data.

The calculation of absorption coefficients using the Gershun approach is complex, so is the quantification of measurement uncertainties. We therefore assessed uncertainties associated with the Gershun approach by propagating standard deviations for measurement at each depth into absorption coefficients using a bootstrap approach, randomly sampling 1000 times assuming normal distributions for all 4 irradiance measurements.

Uncertainty assessments

Quantifying different types of uncertainty

Following the recommendations outlined in the Joint Committee for Guides in Metrology (JCGM 2008), we distinguish between uncertainties associated with random error and those with systematic error. The former, called Type A uncertainty, is calculated as the experimental or observational standard deviation of the arithmetic mean of repeated observations (e.g., burst samples from in situ observations or replicate filter pad samples). This is a convolution of sensor noise and natural variability. The latter, called Type B uncertainty, is evaluated as the positive root of the combined variances associated with each measurement and/or analytic step (e.g., the derivation of a_p from spectrophotometric sample filters or of absorption from uncalibrated transmittance in an AC meter). We will use this as an estimate of measurement variability in specific aspects of protocols and assumptions. By separating the two, we can (1) determine the relative contributions to total uncertainty and (2) determine if the differences between the different approaches are within the uncertainty (and thus not significant) or exceed the uncertainty (and thus are significantly different). The experimental or observational standard deviation of a set of n observations of q_k (in this case, absorption parameters), given by:

$$s(q_k) = \sqrt{\frac{1}{n-1}\sum_{k=1}^{n}(q_k - \overline{q})^2} \cong u_{nat}, \tag{2}$$

where $\overline{q}$ is the arithmetic mean and $n-1$ the degrees of freedom. This will be our estimate of the Type A observational or experimental standard uncertainty associated with sensor noise and natural variability, u_{nat}. The Type B propagated

combined uncertainty, u_c, in parameter y, will be computed from:

$$u_c(y) = \sqrt{\sum_{i=1}^{N} \left(\frac{\partial f}{\partial x_i}\right)^2 u^2(x_i)}, \quad (3)$$

where f is the functional relationship describing the set of N other quantities, x_i, that are related to measurand y (absorption parameter), and $u(x_i)$ is the standard uncertainty for each x_i in f (e.g., uncertainty in filter volume and effective filter area for particulate absorption, or uncertainty in temperature, salinity, and scattering corrections for the AC meters). We will use this to quantify combined uncertainty at what may be considered the current state-of-the-art associated with each approach for estimating absorption. The observational uncertainty associated with natural variability, u_{nat} as defined by Eq. 2 could be one of the x_i terms in the combined uncertainty in Eq. 3. However, because we seek to separate natural variability from operational variability for the purposes of this analysis in order to better compare the methodological uncertainties between approaches, we thus define operational uncertainty u_o, as in Eq. 3 without including the u_{nat} term as in Eq. 2. Specific examples for this calculation are provided in the Supporting Information Appendix S1.

Importantly, the specific factors contributing to uncertainty may be poorly known or unknown. Uncertainty can be quantified without identifying the causes; for example, one can run replicates to obtain a standard deviation without fully knowing all the factors contributing to associated variability. These uncertainty estimates are sometimes reported as 95% confidence intervals (CIs, i.e., 1.96 × standard deviation of replicates or time series) which are expanded uncertainties with a coverage factor of 1.96. CIs aggregate uncertainties from a range of underlying sources of uncertainty, such as natural variability of the sample, lamp stability, consistency of the optical components, detector stability and internal error sources (nonlinearity, stray light), wavelength accuracy, operator consistency (sample handling and storage), temperature, salinity, the presence of bubbles, and, where applicable, variability in particle distributions on filters. However, as already mentioned, uncertainty estimates based on CI or standard deviations do neither provide information on the extent to which different uncertainty terms contribute to the overall observed variability nor reflect systematic uncertainty.

Over the years, key sources of systematic uncertainty have been identified for most approaches and the community has worked to quantify such specific uncertainties and develop methods to correct associated bias. For example, with AC devices three clear sources of systematic uncertainty can be identified: purified water calibrations (analogous to spectrophotometric reference blanks), scattering errors from incomplete light capture using the reflective tube approach, and temperature and salinity dependencies of pure water. However, as with all approaches, there are inevitably factors that are not corrected for at all, perhaps associated with underlying assumptions of the technique or with intermittent instrument drift that is very difficult to characterize. An example of the latter is internal temperature corrections for AC devices implemented in real time through manufacturer software; these temperature dependencies can have hysteresis effects through changing water masses, temporarily causing systematic bias in some cases that is several factors greater than baseline noise (Twardowski et al. 1999). The hope is any such residual variability in any approach may be small. A goal here is assessing relative accuracies (uncertainty normalized to absorption magnitude) of very different approaches with all their specific and inherent uncertainties, some known and some unknown, to provide best possible estimates of true absorption. This is the value in methodological closure exercises such as this study.

Accuracy and uncertainty assessments in spectrophotometry

An instrument's baseline uncertainty associated with instrument noise (without additional natural variability associated with particle scattering, systematic bias errors, etc.) can be assessed following Højerslev (1994). The relative uncertainty associated with instrument noise can be calculated using

$$\left(\frac{\delta a}{a}\right)_{noise} = \frac{dT \times e^{aL}}{aL}, \quad (4)$$

where a is absorption (m^{-1}), δa is the uncertainty associated with instrument noise (m^{-1}), L is the pathlength (m), and dT is the instrumental noise of transmittance measurements (dimensionless) in air. For instruments such as the AC meters, the pathlength is well constrained, while for approaches such as the ISFP, the geometric pathlength is dependent upon the volume filtered and the clearance are of the filter. For ICAM, it is difficult to accurately determine their exact optical pathlength, which varies with turbidity. The instrumental noise of transmittance for an AC meter and benchtop spectrophotometer can easily be determined from laboratory measurements in air, while for PSICAM measurements they will have to be estimated indirectly. The uncertainty associated with instrument noise (m^{-1}) is calculated as:

$$\delta a_{noise} = \frac{dT \times e^{aL}}{L}. \quad (5)$$

This approach allows us to separate baseline uncertainty associated with instrumental noise from experimental uncertainty. Note that when we use the term baseline uncertainty, its meaning is essentially interchangeable with relative or absolute uncertainty due to instrument noise expressed by Eq. 4 or 5.

Comparison of different absorption methods

For consistency, all subsequent analysis and instrument comparisons have been restricted to the visible spectrum, 400–700 nm, because this spectral range is common to all methods. This study uses cross-comparison to evaluate relative operational uncertainties in absorption parameters measured or derived from the different techniques, including a_{nw}, a_{CDOM}, a_p, a_{ph}, and a_{nap} (Table 2). Parameter a_{nw} was measured on the bench top from discrete samples with PSICAM and in situ with the Gershun, AC-s, AC-9, and ICAM approaches. Measurements for a_p were collected with the ISFP methods and QFT-ICAM from filtered discrete samples, and as the difference between a_{nw} and a_{CDOM} from measurements with PSICAM, AC-s, AC-9, and ICAM. Parameter a_{CDOM} was measured on the bench top from filtered discrete samples with the PSICAM and LWCC system, as well as in situ with AC-s, AC-9, and ICAM instruments fitted with a prefilter (Twardowski et al. 1999; Twardowski et al. 2018a); associated AC device data are disregarded, however, in the following due to bubble contamination.

Where available, data sets derived with the same method were compared against each other to test the inherent consistency of the technique, that is, the operational uncertainty within an approach – this was done for the ICAM, AC-9 instruments, and the ISFP approaches. Because there is no absorption standard against which to evaluate the accuracy of all the approaches, we selected one approach against which to evaluate the deviation in absorption parameters, that is, uncertainty between approaches. We chose the PSICAM data as the reference because (1) it provides the most extensive set of absorption parameters (e.g., whole water, filtered water, filter pad samples) and (2) extensive previous work (Röttgers et al. 2005; Röttgers and Doerffer 2007) has demonstrated the PSICAM approach has negligible scattering errors and very low operational uncertainties, partly due to the long effective pathlength of the integrating sphere. The PSICAM thus provides the state-of-the-art estimate of absorption against which the others will be compared. The utility of this approach is that any future improvements in absorption measurement technology can be compared to PSICAM and thus to all other approaches presented here. The difference between each absorption parameter estimate and the PSICAM estimate will be quantified as the difference scaled to the magnitude of the PSICAM-measured absorption (percent difference).

Performance of absorption measurements was assessed by using geometric mean linear regressions for the various data sets and comparative statistics. For completeness, statistics are provided in comparing all method combinations. Regression slope, offset, and the determination coefficient R^2 are a measure of tendency for one parameter to over/underestimate relative to the other parameter, that is, potential systematic differences between parameters. We estimate the differences using parametric and nonparametric approaches depending upon normally distributed and nonnormally distributed errors. When errors may be considered normally distributed, overall uncertainties and accuracies can be quantified by RMSD and percent RMSD (%RMSD), respectively:

$$\mathrm{RMSD} = \sqrt{\frac{1}{\mathrm{m}}\sum_{1}^{\mathrm{m}}\left(\frac{q-q_{\mathrm{ref}}}{q_{\mathrm{ref}}}\right)^2}, \tag{6}$$

$$\%\mathrm{RMSD} = \sqrt{\frac{1}{\mathrm{m}}\sum_{1}^{\mathrm{m}}\left(\frac{q-q_{ref}}{q_{ref}}\times 100\right)^2}, \tag{7}$$

where q is the absorption parameter measured by one instrument and q_{ref} is the absorption parameter measured by another instrument (i.e., PSICAM used as reference, unless otherwise indicated), and m is the number of paired measurements available (in this case, stations). Since there is no approach with zero measurement error, these uncertainties and accuracy assessments are relative to the specific approaches being compared, aggregating both random and systematic errors. Estimates of specific uncertainty sources are provided in the specific method descriptions for the different approaches and are considered in the context of approach comparisons in the Discussion section. In this study, the aim was to (1) quantify the operational uncertainty associated with each measurement approach for a set of absorption parameters, (2) compare that uncertainty to that associated with natural (spatial and temporal) variations, and (3) quantify the differences in absorption parameter estimates between the different approaches with the ultimate goal of understanding and ranking uncertainties associated with each approach to improve the quality of in situ validation for remote sensing.

For the data sets that do not have normally distributed error, nonparametric error assessments such as percentage mean errors, in both absolute and relative terms were used:

$$\delta_{\mathrm{abs}} = \frac{1}{m}\sum\nolimits_{1}^{m}|q-q_{\mathrm{ref}}|, \%\delta_{\mathrm{abs}} = 100\times\frac{\delta_{\mathrm{abs}}}{\overline{q_{\mathrm{ref}}}}, \tag{8}$$

$$\delta_{\mathrm{rel}} = \frac{1}{m}\sum\nolimits_{1}^{m}(q-q_{\mathrm{ref}}), \%\delta_{\mathrm{rel}} = 100\times\frac{\delta_{\mathrm{rel}}}{\overline{q_{\mathrm{ref}}}}, \tag{9}$$

where $\%\delta_{\mathrm{abs}}$ is an aggregate error taking into account the absolute magnitude of the residuals and giving them equal weight and $\%\delta_{\mathrm{rel}}$ is an estimate of the overall biases in the data set, where a value near zero indicates small net bias. Parameters such as %RMSD and $\%\delta_{\mathrm{abs}}$ allow assessment of relative accuracy between measurements. As an example in the application for comparing data from spectrophotometric devices, %RMSD may be most applicable for measurements of a_{CDOM} where data time series may be approximately normally distributed, i.e., with variability coming primarily from sensor noise, where $\%\delta_{\mathrm{abs}}$ may be most appropriate for measurements

Table 4. Summary of suspended particle characterisations for each station. Values of $a_{nap}(440)/a_p(440)$ were obtained with ISFP method (ISFP 2 data set) and $a_p(440)/a_{nw}(440)$ were obtained from PSICAM measurements. The percentage values in parenthesis indicate the coefficient of variation based on duplicate samples.

Station	Date	SPM	POC	Chl *a*	POC : SPM	Chl *a* : SPM	POC : Chl *a*	$a_{nap}(440)/a_p(440)$	$a_p(440)/a_{nw}(440)$
	(DD-MM-YYYY)	(g m^{-3})	(mg m^{-3})	(mg m^{-3})	(g : g)	(g : g)	(g : g)	(–)	(–)
ST01	09 Jan 2017	22.33 (1.36%)	1295.74 (3.35%)	3.94	0.058	1.76 10^{-4}	328.9	0.80	0.74
ST02	09 Jan 2017	9.22 (5.24%)	618.98 (3.37%)	3.62	0.067	3.93 10^{-4}	171.0	0.68	0.43
ST03	09 Jan 2017	15.85 (0.86%)	913.11 (7.24%)	4.43	0.058	2.79 10^{-4}	206.1	0.74	0.73
ST04	10 Jan 2017	22.32 (1.26%)	981.94 (0.02%)	5.39	0.044	2.41 10^{-4}	182.2	0.77	0.85
ST05	10 Jan 2017	4.11 —	392.73 —	4.98	0.096	12.12 10^{-4}	78.9	0.47	0.29
ST06	11 Jan 2017	4.94 (1.00%)	419.61 (2.80%)	2.18 (0.49%)	0.085	4.42 10^{-4}	192.5	0.67	0.57
ST07	11 Jan 2017	6.58 (1.65%)	553.20 (10.67%)	3.64	0.084	5.53 10^{-4}	152.0	0.68	0.50
ST08	12 Jan 2017	4.72 (3.13%)	464.85 (0.45%)	3.28	0.098	6.95 10^{-4}	141.7	0.53	0.35
ST09	12 Jan 2017	—	483.18 (5.83%)	2.18 (1.49%)	—	—	221.6	0.46	0.30
ST10	12 Jan 2017	12.47 (4.99%)	795.47 (0.98%)	2.74	0.064	2.20 10^{-4}	290.3	0.70	0.72
ST11	13 Jan 2017	2.25 (2.01%)	344.72 (1.63%)	3.72 (0.89%)	0.153	16.53 10^{-4}	92.7	0.50	0.25
ST12	13 Jan 2017	3.52 (1.43%)	370.74 (4.26%)	2.53	0.105	7.19 10^{-4}	146.5	0.60	0.30

dominated by particle fields with associated superimposed fluctuations from small scale natural variability.

Results

Characterization of particulate matter

Indian River Lagoon waters are characterized by relatively high concentration of suspended particles. During our experiments SPM ranged between about 2 and 22 g m^{-3}, POC between 340 and 1300 mg m^{-3}, and Chl *a* between 2.2 and 5.4 mg m^{-3} (Table 4). All three concentration metrics are significantly higher than typically observed in open ocean waters (Stramski et al. 2008). The POC/SPM ratio for most samples was very low, below 0.1; the highest observed value was 0.15 at ST11 (Table 4). Such low values are indicative of the dominant contribution of mineral particles to SPM (Woźniak et al. 2010). The Chl *a*/SPM ratio was generally on the order of 10^{-4} with the highest value of 16.5×10^{-4} at ST11 (Table 4). Despite the dominant role of mineral particles, the Chl *a*/SPM ratio is, however, high enough to suggest no major methodological artifacts in the experimental partitioning of a_p into a_{nap} and a_{ph}. It was previously reported that the partitioning method based on pigment bleaching becomes unreliable for samples with very low proportion of phytoplankton in suspended matter when Chl *a*/SPM is less than about 10^{-4} (Woźniak et al. 2010).

Although Chl *a* was moderately high in the examined samples, the relatively low proportion of phytoplankton within the particulate assemblages was supported by data of POC : Chl *a* and the absorption ratio $a_{nap}(440)/a_p(440)$ at the Soret band of Chl *a* (Table 4). The interpretation of POC : Chl *a* in natural waters is confounded by variability in the ratio of phytoplankton carbon (C_{ph}) to Chl *a* and variable contribution to POC from particulate material other than phytoplankton. The limited data of C_{ph} : Chl *a* estimates for phytoplankton in the ocean suggest this ratio can vary within a fairly broad range from about 15 to > 300 with the highest values found in oligotrophic waters and the lowest values in

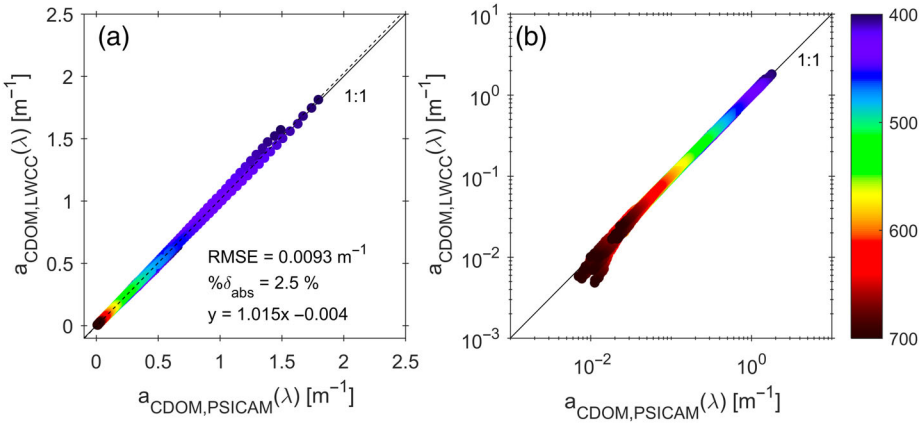

Fig 3. Comparison of CDOM absorption, a_{CDOM}, measurements made with LWCC and PSICAM for all stations, on (**a**) a linear scale and (**b**) a log–log scale. Color of circles represents wavelength from 400 to 700 nm.

upwelling and temperate waters and coastal environments (Sathyendranath et al. 2009; Graff et al. 2015). Given our data were collected in relatively turbid coastal waters with high Chl *a*, the magnitude of POC : Chl *a* from about 75 to 330 appear to indicate significant contribution of nonphytoplankton carbon to POC.

Finally, the $a_{nap}(440)/a_p(440)$ ratio was generally higher than typical values observed in the open ocean (Bricaud and Stramski 1990), which further supports the notion of limited proportion of phytoplankton within the examined particulate assemblages. This characterization of SPM explains the observed spectral shapes of a_p shown in Particulate absorption a_p section, which are typical for samples with weakly pronounced absorption features of phytoplankton but dominated by nonalgal particulate absorption with major contribution of mineral particles (Babin et al. 2003; Babin and Stramski 2004; Bowers and Binding 2006). The relative contribution of particulate absorption to overall absorption varied widely across samples stations from 0.25 at ST11 to 0.85 at ST04.

CDOM absorption a_{CDOM}

Measurements of a_{CDOM}, that is, absorption by material passing through a 0.2-μm filter, are generally considered the most accurate because, due to the nature of the sample, particle scattering effects are considered negligible. In this study, a_{CDOM} was measured in situ with the ICAM and from discrete samples with the PSICAM, LWCC, and dual-beam spectrophotometer. A summary of cross-comparison of each method against every other is given in Supporting Information Table S1.

Comparison of a_{CDOM} measured with the bench-top LWCC and PSICAM showed good agreement (%δ_{abs} = 2.5%) and small tendency for LWCC to overestimate PSICAM absorption with a slope of 1.015 (± 0.001) (Figs. 2, 3). Largest relative deviations were observed at longer wavelengths, presumably

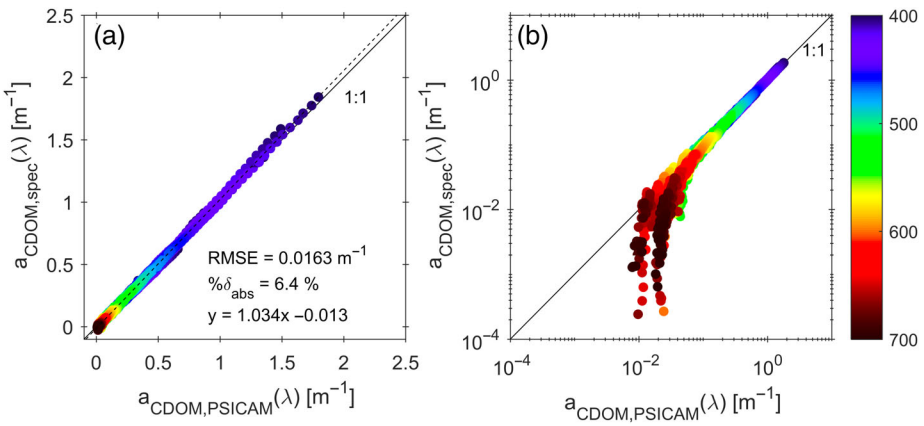

Fig 4. Comparison of CDOM absorption, a_{CDOM}, measurements made with a dual beam-spectrophotometer equipped with a 10-cm cuvette and the PSICAM for all stations, on (**a**) a linear scale and (**b**) a log–log scale. Color of circles represents wavelength from 400 to 700 nm and the 1 : 1 line (solid) and linear regression line (dashed).

driven by scaling, that is, small absolute errors result in large relative errors when absorption is low. Alternatively, the deviation could originate from residual temperature and salinity effects if not fully corrected. The agreement had been significantly improved by correcting data from both instruments for detector issues, including nonlinearity, internal stray light, and issues with spectral registration (data not shown). The calibration determining the reflectivity of the PSICAM's cavity walls uses LWCC data, and thus the interdetector variability will not include those systematic errors. However, PSICAM calibration, using a highly concentrated colored solution in purified water, is not affected by scattering or salinity effects and sensitivity issues are negligible. In addition, LWCC absorption coefficients reported in this study take into account measurements from two independent LWCC systems (with different pathlength cells) reducing any potential covariance between PSICAM and LWCC a_{CDOM} due to errors in the true LWCC pathlength. Furthermore, both measurements are affected by a range of different independent factors, such as lamp stability, sample to sample variation, salinity dependent refractive index corrections, and detector sensitivity, so they may be considered independent measurements.

Measurements of a_{CDOM} in a 10-cm cuvette with the dual-beam spectrophotometer showed overall good agreement with

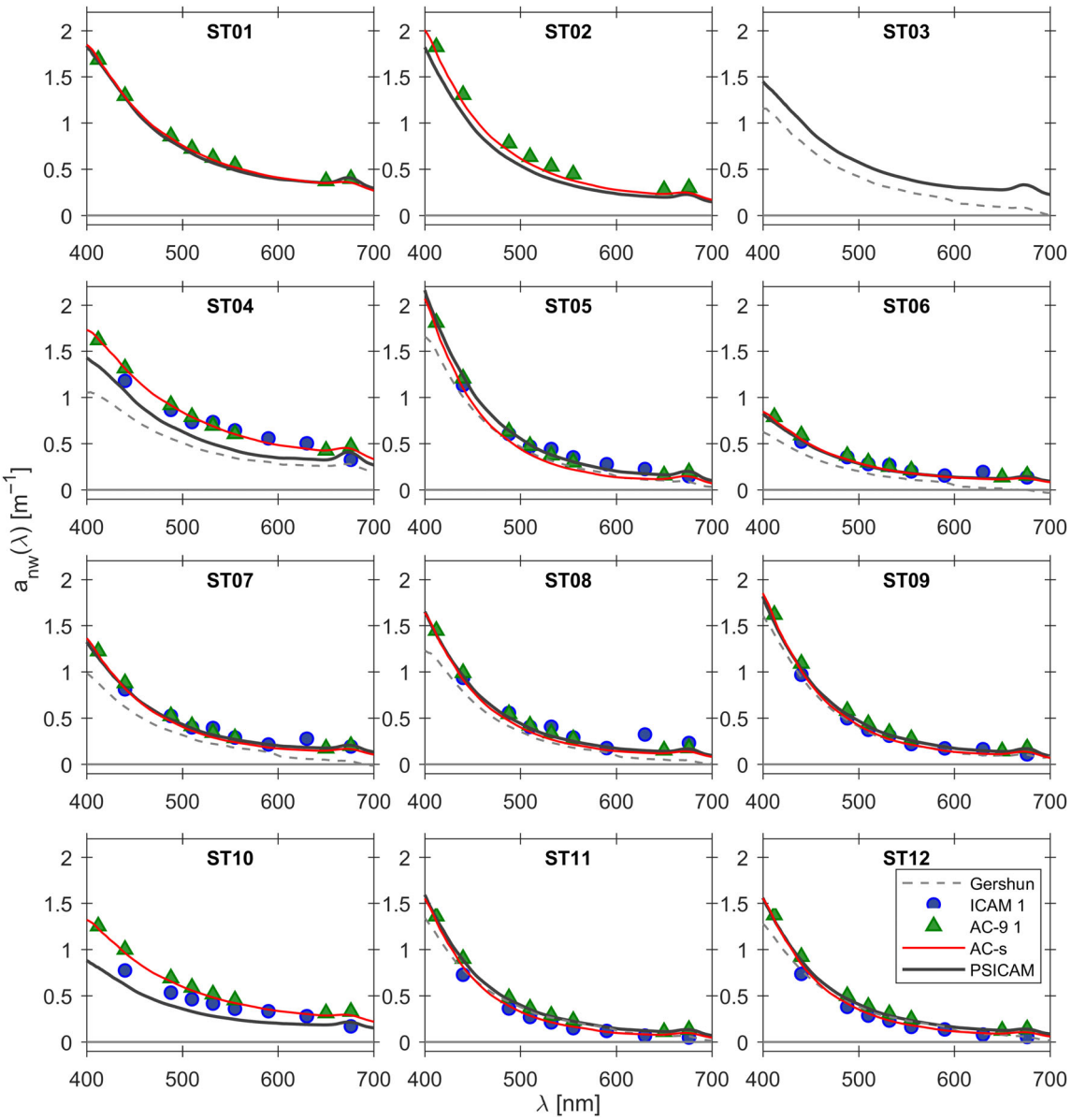

Fig 5. Nonwater absorption spectra, a_{nw}, measured using ICAM 1, PSICAM, AC-s, AC-9 1, and derived from measurements of the irradiance quartet using Gershun's law. No ICAM, AC-9, or AC-s data were collected at Sta. 3.

the other two benchtop methods (Fig. 2), with a 6.5% $\%\delta_{abs}$ when compared to PSICAM a_{CDOM} (Fig. 4). The slightly larger degree of variability compared to the LWCC vs. PSICAM comparison can likely be explained by the method's significantly shorter optical pathlength of 10 cm, limiting the sensitivity, as well as small differences in data processing. Results also indicate a loss of sensitivity of the PSICAM in the NIR whereas the spectrophotometer resolves nearly two orders of magnitude lower values. LWCC data were offset corrected at 700 nm while spectrophotometer data were not because they were within the range of instrument noise of zero indicating negligible scattering error.

Agreement between PSICAM and the multispectral ICAM1 and ICAM 2 instruments measuring a_{CDOM} in situ exhibited larger deviations compared to the discrete measurements, with $\%\delta_{abs} > 35\%$ and generally increasing with wavelength (Fig. 2). The deviations between the ICAM and PSICAM were highly variable across different stations suggesting that it was not due to a systematic bias, but simply high variability in ICAM measurements. For the one sample where a_{CDOM} data were available from both ICAMs, $\%\delta_{abs}$ was 23% (Supporting Information Table S1).

Nonwater absorption a_{nw}

A summary of cross-comparison of each method against every other for the total nonwater absorption coefficient, a_{nw}, is given in Supporting Information Table S2. At Stas. ST01, ST03, ST04, and ST10, a_{nw} was dominated by particulate matter with relative contributions of $a_p > 70\%$ (Table 4). Conversely, a_{CDOM} was the dominating contributor (≥ 70%) to a_{nw} at ST05, ST09, ST11, and ST12.

The agreement between the two ICAMS and the PSICAM was higher for a_{nw} than for a_{CDOM} (Fig. 5). This further emphasizes the likelihood of contamination of the in situ a_{CDOM} measurements by bubbles originating from the inline filters and the difficulties in completely degassing flow cells in very shallow waters. With the exception of the Gershun method, measurements showed a small tendency to overestimate PSICAM absorption with slopes within 10% of 1.0 and $\%\delta_{abs} < 20\%$, with exception of ICAM 2. Slight overestimation likely related to residual bias associated with scattering effects but may be due to the inclusion of more large particles that are relatively rare, as time averaging results in larger effective sample volumes. Approximately, 60% of R^2 values for the 42 comparisons were > 0.95, indicating strong linear relationships between the instruments and generally consistent spectral shapes, although because many systematic errors scale with magnitude, they may not be a constant contribution to uncertainty but to % error. Lowest R^2 of 0.83 was observed for ICAM 1 vs. Gershun. Detailed analysis is provided below.

ICAM a_{nw} and a_{CDOM}

Only a small number of simultaneous measurements with two ICAMs were available and, hence, a_{nw} ($n = 2$) and a_{CDOM} ($n = 1$) were combined for analysis (details on separate analysis of a_{CDOM} and a_{nw} can be found in Supporting Information Tables S1, S2, respectively). ICAM measurements were relatively precise in the visible range ($\%\delta_{abs} < 17\%$), with a small tendency of ICAM 1 to underestimate ICAM 2 at longer wavelengths (slope = 1.065 [± 0.045]; Fig. 6). The linear regression model showed both ICAM a_{nw} data sets were on average not significantly different from PSICAM data. However, the average spread in the a_{CDOM} and a_{nw} data was 27%, and discrepancies for individual wavelengths were not consistent ($\%\delta_{abs}$; Fig. 7). These measurement discrepancies between wavelengths from sample to sample suggest inherent instabilities in the ICAM; however, the more consistent agreement between the two ICAMs suggests there may in fact be systematic errors afflicting both ICAMs.

ICAM a_{CDOM} tended to underestimate PSICAM values, while a_{nw} was predominantly overestimated relative to PSICAM data. Despite the fact that no attempt was made to correct ICAM data for scattering effects, agreement with

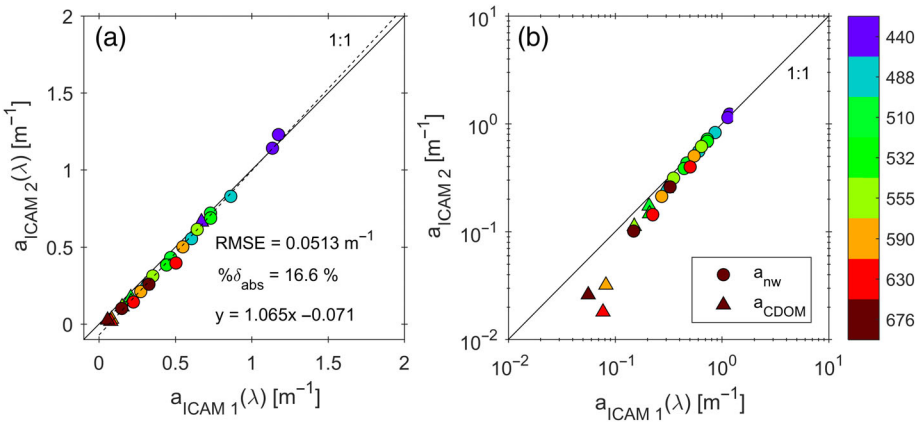

Fig 6. Comparison of a_{nw} and a_{CDOM} measured by two ICAMs mounted on the same frame ($n = 3$), on (**a**) a linear scale and (**b**) a log–log scale, with the 1 : 1 line (solid) and linear regression line (dashed). Note that metrics of agreement are given for the combined a_{nw} and a_{CDOM} data set.

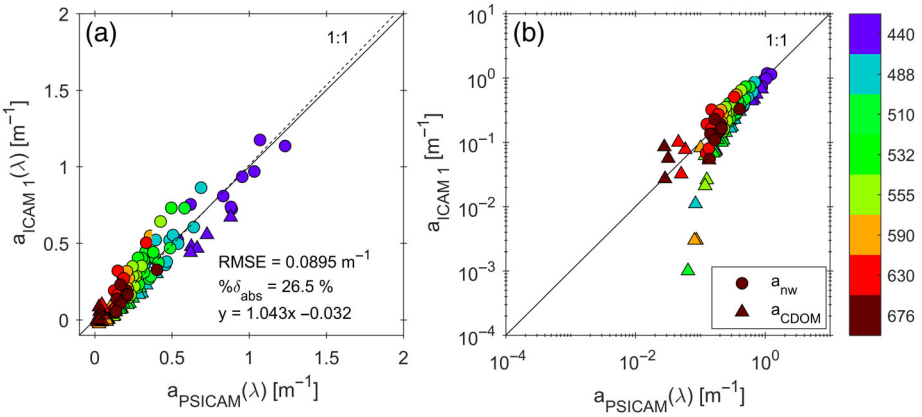

Fig 7. Comparison of a_{nw} and a_{CDOM} measured with an ICAM compared to measurements with a PSICAM ($n = 15$) for eight ICAM wavebands in the visible spectrum (440, 488, 510, 532, 555, 590, 630, 676), on (**a**) a linear scale and (**b**) a log–log scale, with the 1:1 line (solid) and linear regression line (dashed). Note that measures of agreement are given for the combined a_{nw} and a_{CDOM} data set.

PSICAM for ICAM 1 a_{nw} was broadly consistent with AC-s and the two AC-9 instruments with $\%\delta_{abs} < 20\%$, although slopes deviated within 11% from unity.

AC-9 and AC-s a_{nw} *and* a_{CDOM}

As expected, the agreement between different AC-9 and AC-s instruments and other sensors was strongly dependent

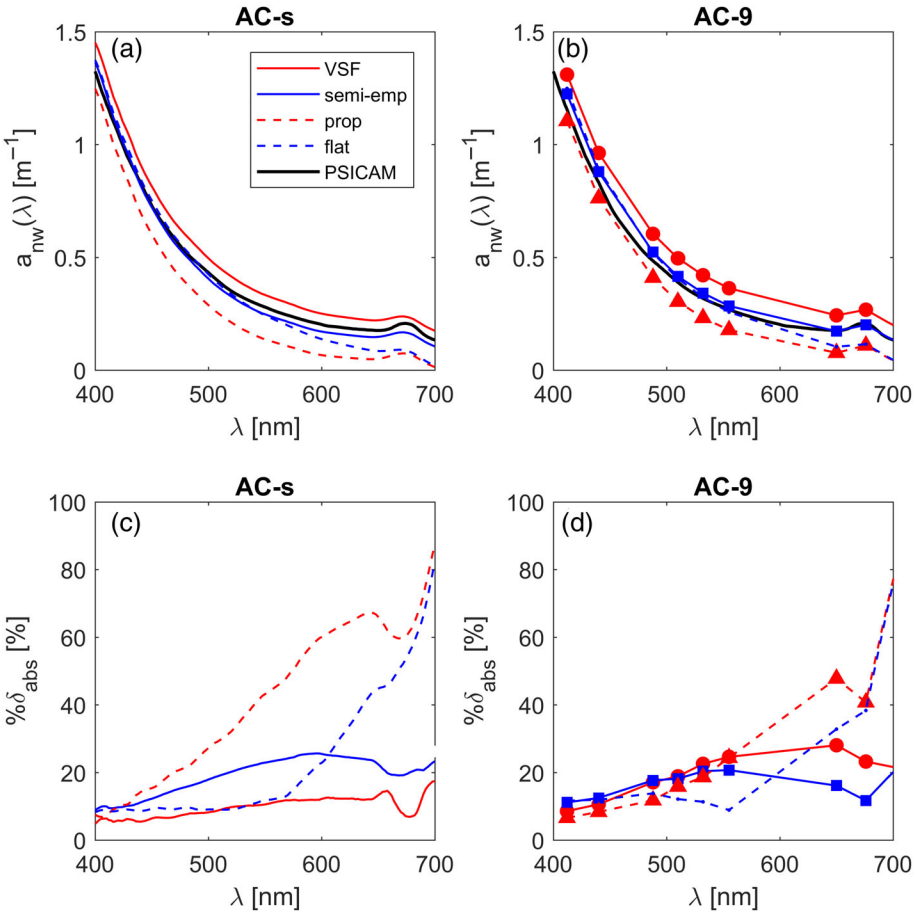

Fig 8. Effect of different scattering corrections on total nonwater spectral absorption a_{nw} measured at ST07 in (**a**) AC-s and (**b**) AC-9 measurements. For comparison, PSICAM absorption spectra are shown in black. Spectral average $\%\delta_{abs}$ shown for (**c**) AC-s and (**d**) AC-9 measurements. Scattering corrections include the independent VSF-based correction (Stockley et al. 2017), semiempirical correction (Röttgers et al. 2013), proportional and flat (or baseline) corrections from Zaneveld et al. (1994).

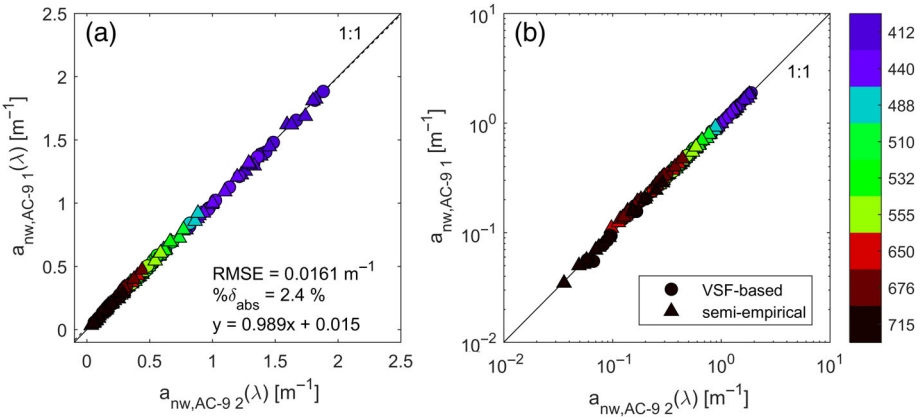

Fig 9. Comparison of nonwater absorption a_{nw} data measured with two AC-9 (n = 11) instruments mounted on the same frame, on (**a**) a linear scale and (**b**) a log–log scale, with the 1 : 1 line (solid) and linear regression line (dashed). Data have been corrected for scattering errors using two different correction approaches: The semiempirical method (Röttgers et al. 2013) and an approach using independent VSF data (Stockley et al. 2017). Regression coefficients, RMSD and %δ_{abs} are shown for data correction with semiempirical correction.

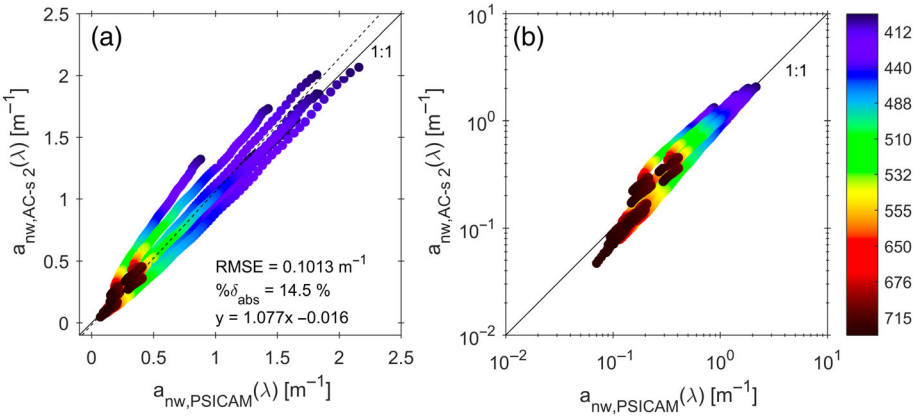

Fig 10. Comparison of total nonwater absorption a_{nw} data measured with an AC-s against PSICAM absorption data (n = 11, 400–700 nm), on (**a**) a linear scale and (**b**) a log–log scale, with the 1 : 1 line (solid) and linear regression line (dashed). AC-s data have been corrected for scattering errors using the semiempirical method (Röttgers et al. 2013).

on the choice of scattering correction for the AC devices. Figure 8 shows the effect of the four different scattering correction approaches on AC-9 and AC-s a_{nw} data collected at ST07 compared to PSICAM measurements. The scattering corrections not assuming zero absorption in NIR spectral region, that is, the semiempirical correction from Röttgers et al. (2013) and the independent VSF-based correction (Stockley et al. 2017; Tonizzo et al. 2017), generally performed better in the complex case 2 waters of this study (Fig. 8). However, note remaining errors at longer wavelengths can still be > 20%. No consistent trend could be observed when comparing the semiempirical vs. VSF corrections, that is, sometimes VSF correction outperformed the semiempirical correction and vice versa when compared with PSICAM data. However, VSF data were not available for all stations, so we therefore used the semiempirical correction for all subsequent analysis in this paper, including a_{nw} in Fig. 5.

Data from the two independent AC-9 devices were found to be very consistent, with %δ_{abs} < 3% and a slope of 1.011 (± 0.006) (Fig. 9). AC-9 and AC-s were on average also very consistent across all wavelengths (regression slope: 1.005 [± 0.013]) but showed a higher %δ_{abs} of 8%. Results from the semiempirical and VSF-based corrections were remarkably consistent, with %δ_{abs} < 9.7% for AC-s and both AC-9 instruments. Across the entire spectrum, both AC-9 and AC-s a_{nw} data agree with the PSICAM within %δ_{abs} = ±15%. Deviations between AC-9 and AC-s with respect to PSICAM vary on a sample by sample basis, typically increasing toward blue wavelengths in absolute numbers and toward the NIR region in relative terms (Figs. 10 and 11).

Total absorption a_t measurements with Gershun method

Hyperspectral total absorption coefficients were calculated from radiometric measurements of the irradiance quartet

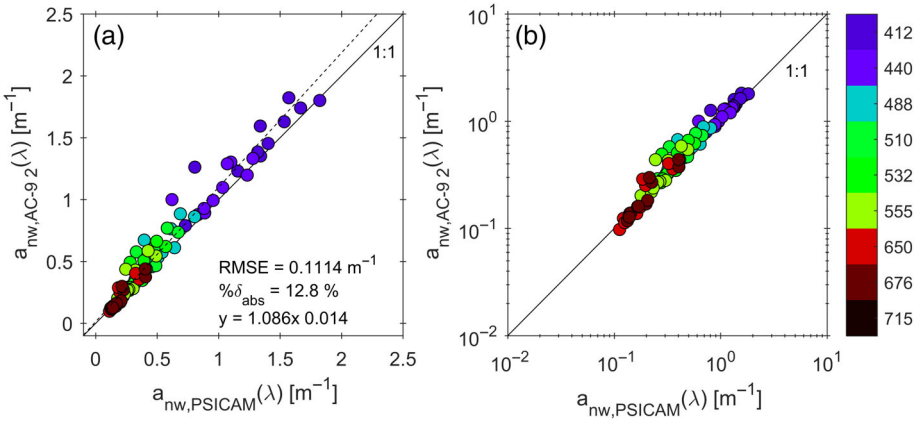

Fig 11. Comparison of nonwater absorption a_{nw} data measured with an AC-9 instrument against PSICAM absorption data ($n = 12$) at nine AC-9 wavelengths, on (**a**) a linear scale and (**b**) a log–log scale, with the 1 : 1 line (solid) and linear regression line (dashed). AC-9 data have been corrected for scattering errors using the semiempirical method (Röttgers et al. 2013).

using Gershun's equation. Gershun a_{nw} (with the water contribution subtracted from the derived total spectral absorption coefficient) was the only method that consistently underestimated PSICAM data with deviations increasing toward both edges of the spectrum (Fig. 12).

To investigate whether inelastic scattering effects could potentially explain some of the deviation observed in data obtained with the Gershun method compared with PSICAM data, we calculated Gershun absorption spectra from underwater light fields simulated with the Hydrolight (Numerical Optics, UK) radiative transfer model, both with and without inelastic effects. The model inputs are the inherent optical properties, specifically AC-s a_{nw} and c_{nw} data, LWCC a_{CDOM} data, ECO-BB3 b_{bp} data (interpolated and extrapolated to cover full visible range) and the Chl *a* concentrations. Hydrolight uses these data to estimate total absorption, total attenuation, total scattering, total backscattering, CDOM fluorescence and Chl *a* fluorescence at the desired wavelength resolution and to subsequently simulate radiometric fields. CTD temperature and salinity data were used to correct pure water absorption values. Skylight was modeled with the default configuration of the built-in algorithm RADTRAN. Results for ST04 demonstrated that inelastic radiative effects (Raman scattering by water molecules, chlorophyll fluorescence and CDOM fluorescence) were negligible in these turbid waters and shallow depths and not able to explain the discrepancies with PSICAM data (data not shown).

To test if random errors in depth measurements of up to ±20 cm were able to explain discrepancies between Gershun and PSICAM absorption spectra, a bootstrapping exercise was carried out. For each profile, absorption was derived with the Gershun method with 1000 random depth offsets in the ±20 cm range added to each measurement, assuming normal distributions for all four irradiance measurements. The best match was subsequently identified with corresponding PSICAM measurements through minimization of %δ_{abs}. Figure 13 shows that potential uncertainties in depth readings

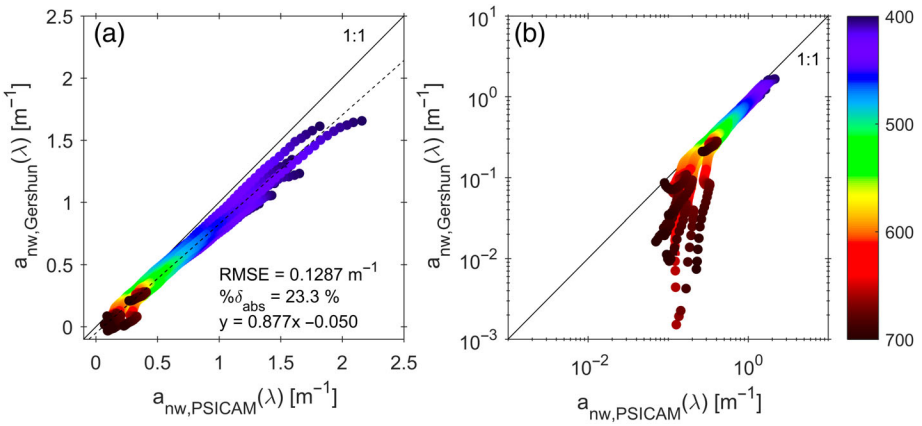

Fig 12. Comparison of nonwater absorption, a_{nw}, data derived from radiometric data using Gershun's law compared to measurements with a PSICAM (400–700 nm), on (**a**) a linear scale and (**b**) a log–log scale, with the 1 : 1 line (solid) and linear regression line (dashed). Color of circles represents wavelength from 400 to 700 nm.

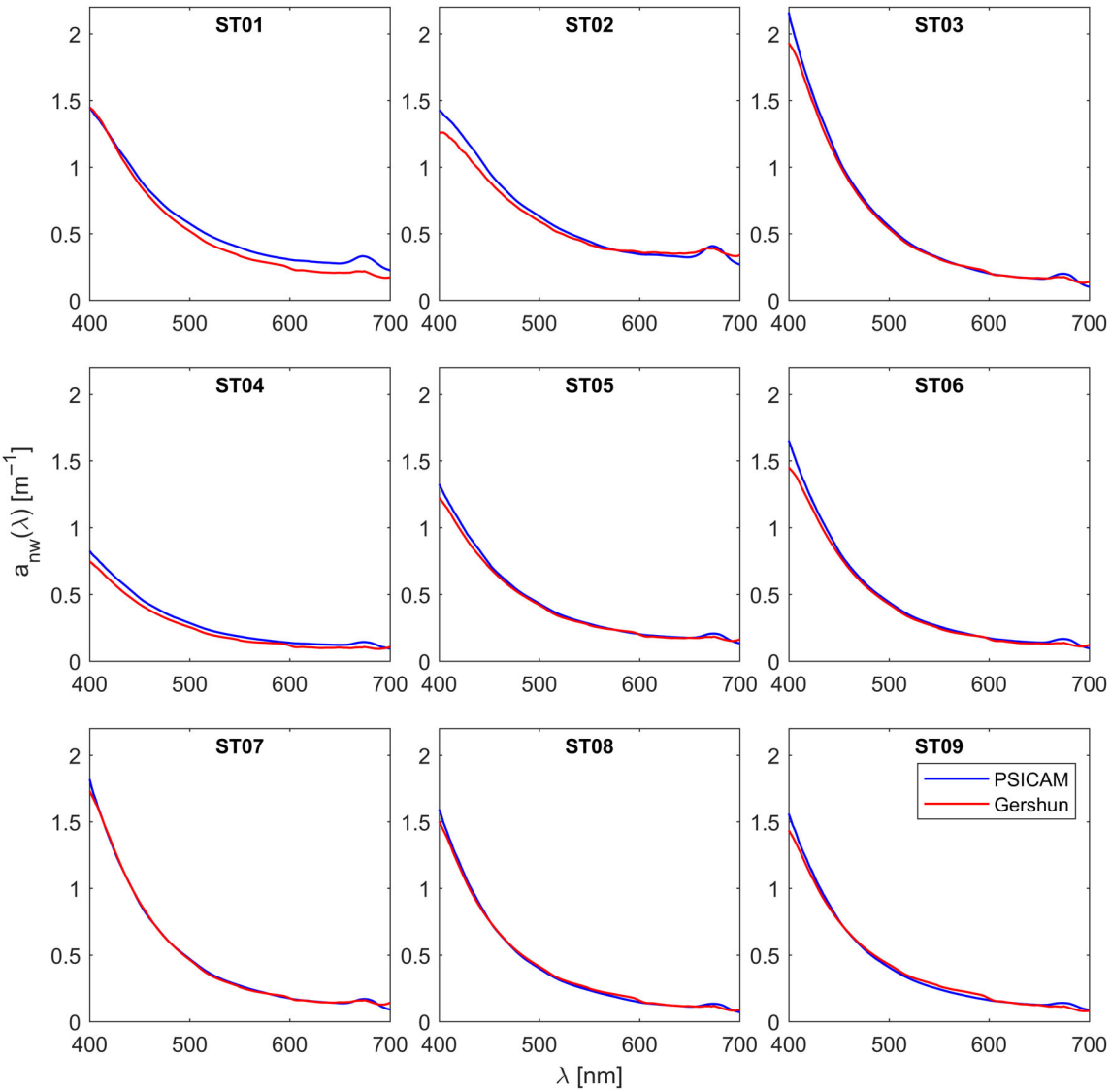

Fig 13. Best agreement between Gershun and PSICAM nonwater absorption, a_{nw}, data from bootstrap experiment allowing 20 cm random uncertainty in depth recording.

within ±20 cm could account for almost all deviation between PSICAM and Gershun-derived absorption data. Between 400 and 550 nm, the correction increased Gershun-derived a_{nw} by a constant factor varying between 6% and 25% of corresponding PSICAM absorption depending on the sample. At longer wavelengths the effect of the correction increased to > 100%. Resulting $\%\delta_{abs}$ in match ups for the nine stations ranged between 1.4% and 10.6%.

Shapes of Gershun absorption spectra exhibited some unexpected features, namely: (1) chlorophyll absorption peaks present in PSICAM absorption spectra (and spectra from other methods) around 675 nm were often substantially dampened, possibly influenced by chlorophyll fluorescence; and (2) subtle residual pure water absorption features were sometimes apparent (Fig. 13). While the exact source of these features could not be determined, it is likely that measurements at longer wavelengths were photon-limited (the Gershun method is a passive approach, without an artificial light source) and, hence, poorly resolved. Residual features resembling pure water absorption could also potentially be explained by insufficient correction of salinity and temperature effects during data processing.

Particulate absorption a_p

Laboratory measurements of a_p for discrete samples were conducted with the filter pad technique using two different set-ups, the postcruise ISFP measurements in two different labs using frozen and stored sample filters and on-board QFT-ICAM measurements on freshly prepared filters immediately after sample collection. In situ data were available from ICAM, where a_p was calculated as the difference between separate a_{nw} and a_{CDOM}

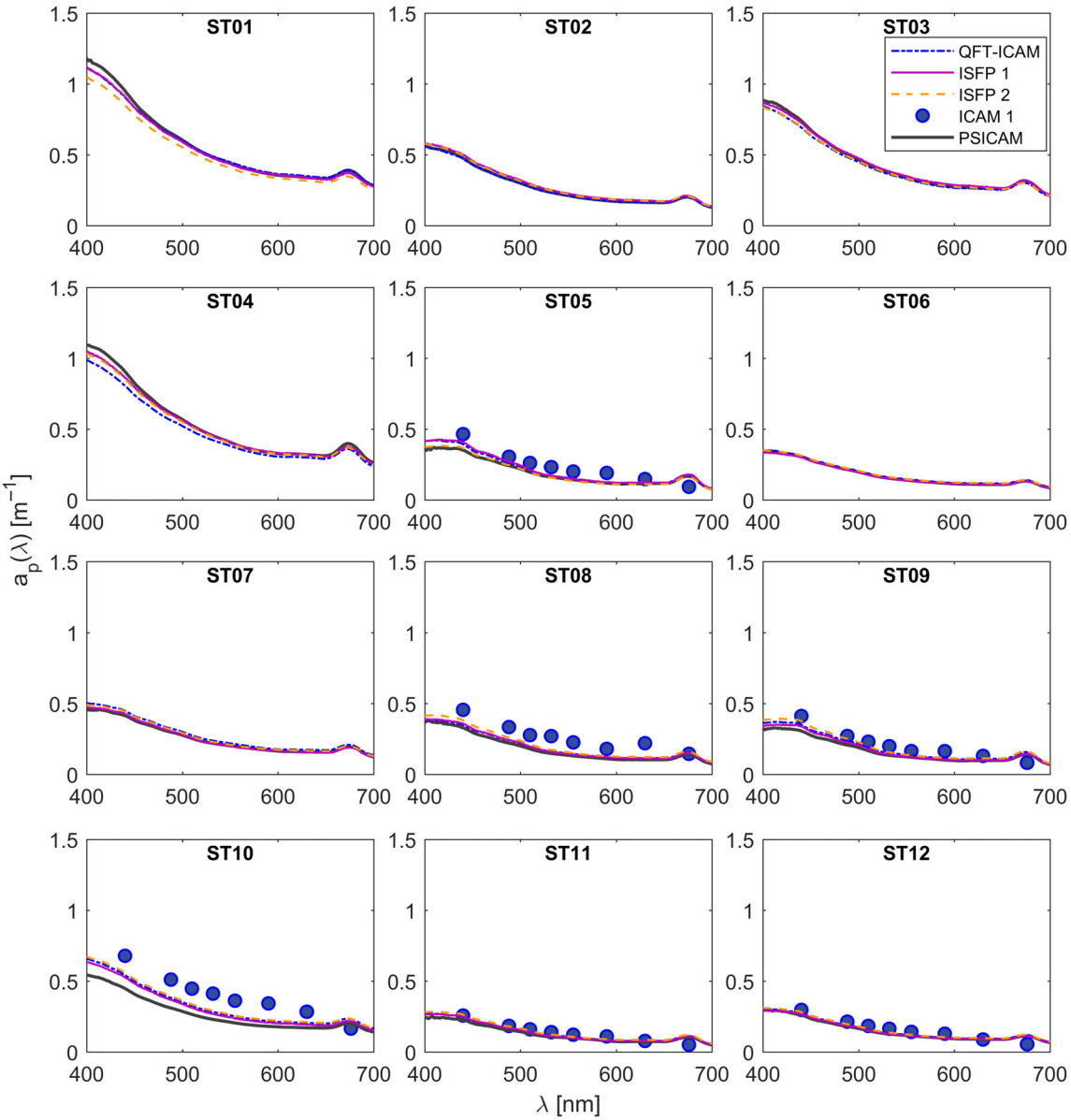

Fig 14. Particulate absorption spectra measured using various approaches for all stations. ICAM a_{CDOM}, and as a result a_{nw} data were available for only 6 out of 12 stations.

measurements. For comparison, PSICAM a_p was also calculated from separate a_{nw} and a_{CDOM} measurements on discrete samples. Supporting Information Table S3 shows a summary of the agreement between different absorption parameters with spectra plotted in Fig. 14. ISFP and QFT-ICAM methods generally showed smaller differences than in situ methods, with smaller uncertainties in the regression coefficients and lower $\%\delta_{abs}$ in comparisons with PSICAM data, that is, < 10% for filter pad methods vs. > 15% for in situ measurements (Supporting Information Table S3). The agreement between the two ICAMs improved slightly for the a_p comparison relative to a_{nw}.

***ISFP approaches* a_p**

The two data sets were found to be very consistent with $\%\delta_{abs}$ equal to 5.4% for a_p and 6.5% for a_{nap} (Fig. 15). Strong linear correlations were observed with $R^2 > 0.99$ for each individual sample in ISFP 1 and ISFP 2 a_p comparisons, although regression slopes varied from sample to sample in the range 0.894 to 1.115 (Fig. 15). The average slope for all stations was 0.954 ($\pm$ 0.004). This suggests the discrepancy between the two methods can be explained by a single factor that is not dependent on wavelength or OD (signal strength or filter pad loading).

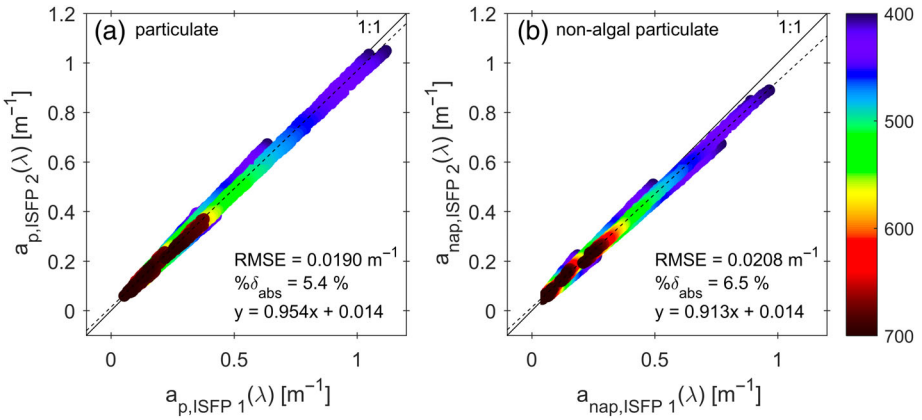

Fig 15. Comparison of (**a**) particulate and (**b**) nonalgal particle absorption data measured by two different labs using two independent filter pad measurements based on the ISFP approach (400–700 nm), with the 1 : 1 line (solid) and linear regression line (dashed).

The level of agreement between the two ISFP approaches sample to sample was broadly comparable for an a_{nap} and a_p. With regard to a_{ph} (data not shown), data from the two ISFP measurements were slightly less strongly correlated showing small hysteresis effects at shorter wavelengths, with $R^2 = 0.9690$ and an average slope of 1.069 ($\pm$ 0.022). As expected, there was also a slightly wider spread in a_{ph} with $\%\delta_{abs}$ 11.6% and RMSD 0.0113 m^{-1} compared to a_p and a_{nap} because a_{ph} was derived as the difference of these two parameters. The observed overall offset determined from linear regression through all a_{ph} data was 0.002 ($\pm$ 0.002) m^{-1}, smaller than offsets for either a_{nap} or a_p (0.014 [$\pm$ 0.001] m^{-1}), suggesting that systematic errors have, to some extent, canceled out during subtraction.

ISFP and QFT-ICAM a_p

ISFP 1 and ISFP 2 a_p data agreed with onsite QFT-ICAM data to a comparable degree ($\%\delta_{abs} < 5\%$). Both systematic and random errors, thus, appear small. Again, strong correlations ($R^2 > 0.99$) were observed for each sample, but with regression slopes from sample to sample that varied between 0.971 and 1.070 (Fig. 16). ISFP 1, ISFP 2, and QFT-ICAM data sets compared similarly to PSICAM a_p ($\%\delta_{abs} < 7.5\%$), with QFT-ICAM a_p showing slightly more variability both spectrally and across stations (Fig. 17; Supporting Information Table S3).

ICAM a_p

The a_p determined in situ by difference between unfiltered and filtered observations with in the ICAM are consistently larger than those determined on filter pads. One of the most obvious reasons for this is that the ICAM was filtered in situ with a 0.2-μm cartridge filter, while the filter pads used for the other measurements on GF/F filters have nominal pore size of 0.7 μm. Spectrophotometric analysis of filtrate from 0.2- and 0.7-μm filters reveals that the absorption within that pore size interval for these samples varies from negligible to approximately 0.05 m^{-1} at 400 nm, decaying exponentially toward the red end of the spectrum (data not shown). The absorption measured in this size interval was consistent with the ICAM overestimation of the GF/F measurements. One notable

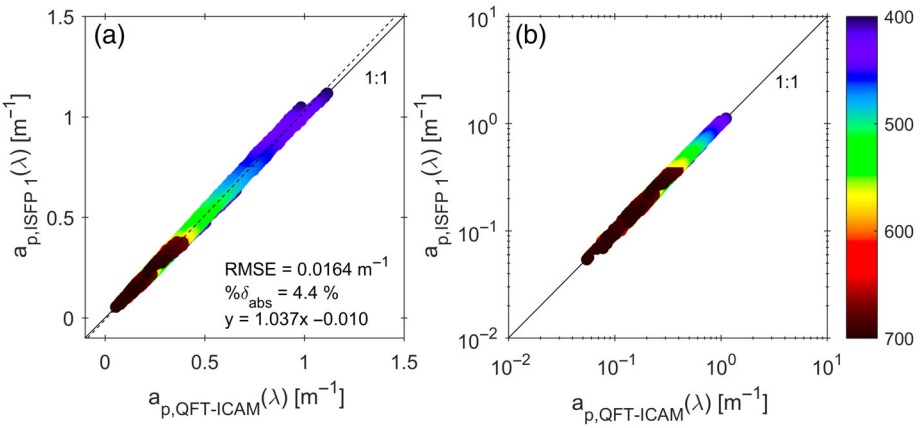

Fig 16. Comparison of particulate absorption data, a_p,measured by two different labs using different filter pad methods, ISFP 1 approach and QFT-ICAM (400–700 nm), on **(a)** a linear scale and (**b**) a log–log scale, with the 1 : 1 line (solid) and linear regression line (dashed).

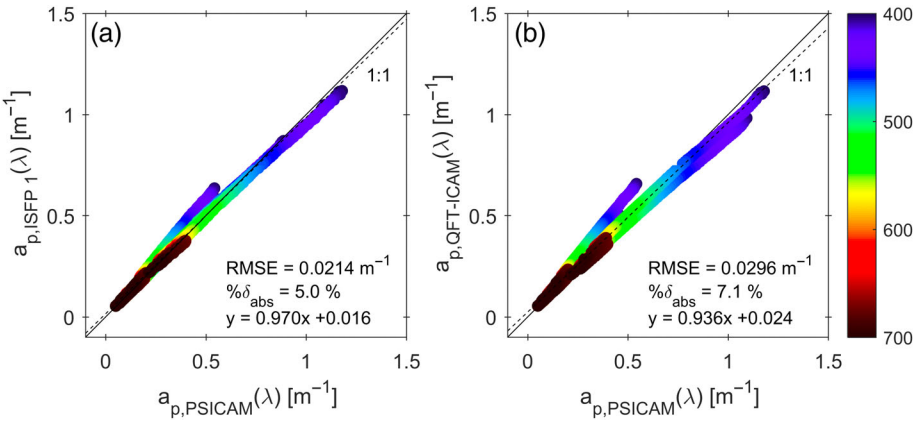

Fig 17. Comparison of particulate absorption data measured by two different labs using different filter pad methods, (**a**) ISFP approach and (**b**) QFT-ICAM, both vs. a_p derived from $a_{nw} - a_{CDOM}$ from PSICAM measurements from 400 to 700 nm. Also shown are 1 : 1 line (solid) and linear regression line (dashed).

exception was observed in the 676 nm channel, where the ICAM data display no red absorption peak associated with Chl *a*, as was clearly identifiable in the spectra obtained on the filter pads.

Confidence intervals

Average CIs, or expanded uncertainties, were wavelength dependent for all absorption methods with generally the largest absolute uncertainties at shorter wavelengths, following the shape of the corresponding absorption spectrum. Relative average CIs, on the other hand, were greatest at red wavelengths. Overall uncertainties for Gershun-derived absorption spectra (derived using the bootstrap approach) were extremely large, > 0.13 m^{-1} across all wavelengths with values increasing toward both edges of the spectrum, exhibiting both water and nonwater absorption features (Fig. 18). The magnitude of Gershun CI reflects the challenges with accurate depth measurement, fluctuations in the underlying radiometric measurements, and computation of absorption spectra (Fig. 18a). AC-s and AC-9 CI were virtually identical demonstrating very consistent performance across different AC instruments. Larger CI for AC-s measurements of a_{CDOM} with respect to a_{nw} provided additional evidence that AC-s measurements were potentially affected by bubbles (data not shown). Conversely, ICAM a_{CDOM} uncertainties were lower than a_{nw} uncertainties suggesting that if bubbles were present, the effect on absorption measurements was small.

Spectrally, PSICAM (a_{nw} and a_{CDOM}) and LWCC (a_{CDOM}) average CIs followed the shape of the corresponding absorption spectra, showing errors scale with magnitude to a large degree. In relative terms, mean CIs were within 5% of the measured signals for wavelengths < 600 nm. At longer wavelengths, CIs increased to 16% for a_{CDOM} (both LWCC and PSICAM) and 6% for PSCIAM a_{nw}. CIs were very consistent across the different filter pad absorption methods, ISFP and QFT-ICAM, with little variability across the spectrum and maximum values of 0.025 m^{-1} at 400 nm. Notably, PSICAM CIs for a_{nw} show a significant increase in the blue relative to other methods due to decreased signal caused by high absorption with long effective pathlength in the integrating cavity.

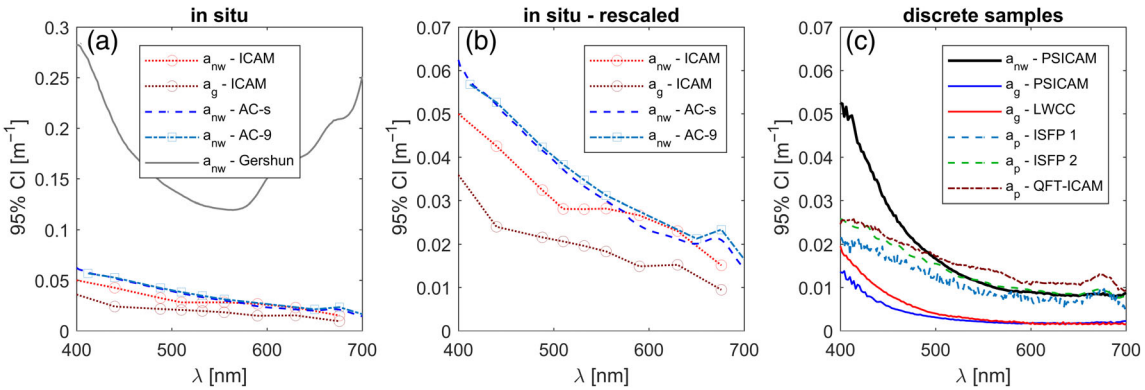

Fig 18. 95% Confidence intervals (= 1.96 * standard deviation of individual time series or replicate measurements) for different spectral absorption measurements (**a**) in situ, (**b**) same as (**a**) but on a different scale with Gershun data removed and (**c**) from discrete sample measurements.

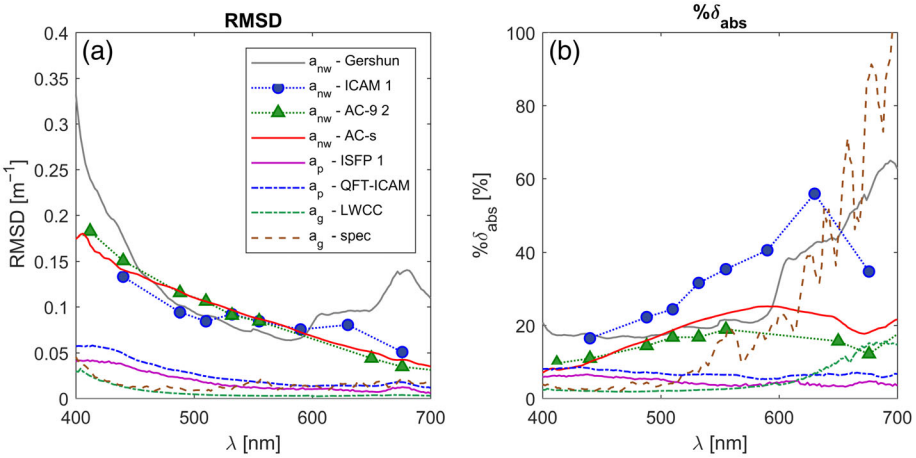

Fig 19. **(a)** RMSD and **(b)** %δ_{abs} as function of wavelength for different absorption measurements in comparison to the PSICAM (LWCC: a_{CDOM}; ISFP & QFT-ICAM: a_p; AC-s, ICAM, Gershun: a_{nw}).

Discussion

Spectral absorption by marine water is the key parameter linking ocean color remote sensing to phytoplankton pigment composition, phytoplankton diversity, algal biomass, and ocean primary productivity. Key algorithms to derive spectral absorption of oceanic constituents from ocean color remote sensing rely in some way on empirical data sets of absorption measurements (Roesler and Perry 1995; Lee et al. 2002; Werdell et al. 2013, 2018). Furthermore, accurate absorption data are required for validation of inverse reflectance models for estimating inherent optical properties (IOPs), (Loisel et al. 2018; Twardowski and Tonizzo 2018). These algorithms are developed based on radiative transfer simulations. Relative uncertainties in absorption data thus underpin accuracies associated with these algorithms. Specifically, significantly improved uncertainties for in situ absorption measurements are needed for the PACE mission from the UV to NIR (PACE Science Team Gaps Matrix, https://pace.oceansciences.org/docs/pace_gaps_iop.pdf), as well as the capability to resolve absorption with respect to depth and continuously in flow-through systems while a ship is underway (IOCCG Protocol Series—Vol. 4.0, 2019*b*). Beyond ocean color remote sensing, knowledge of uncertainties in absorption measurements is important in the interpretation of a range of other models relying on absorption as an input parameter, for example, in bio-optical, biogeochemical, primary production, heat flux, and ecosystem models.

Absorption coefficients in natural waters are one of the most difficult optical properties to measure because scattering by suspended particles leads to overestimation either directly

Table 5. RMSD and %δ_{abs} for comparison of absorption data from different sensors with PSICAM absorption at 440, 555, and 676 nm—plus range of absorption coefficients as measured with the PSICAM at these three wavebands.

	Sample type	RMSD @ 440 nm (m^{-1})	RMSD @ 555 nm (m^{-1})	RMSD @ 676 nm (m^{-1})	%δ_{abs} @ 440 nm (%)	%δ_{abs} @ 555 nm (%)	%δ_{abs} @ 676 nm (%)
Absorption range:	a_{nw}	0.40–1.32	0.11–0.64	0.05–0.47			
ICAM	a_{nw}	0.1332	0.0845	0.0508	16.5	35.4	34.7
AC-9	a_{nw}	0.1506	0.0846	0.0346	10.9	18.9	12.2
AC-s	a_{nw}	0.1396	0.0874	0.0423	10.0	23.1	18.0
Gershun	a_{nw}	0.1766	0.0746	0.1381	17.6	21.6	55.7
Absorption range:	a_p	0.25–0.91	0.10–0.44	0.11–0.39			
ISFP	a_p	0.0371	0.0118	0.0123	6.4	3.7	4.7
QFT-ICAM	a_p	0.0494	0.0179	0.0178	8.2	6.5	6.7
Absorption range:	a_{CDOM}	0.08–0.88	−0.01-0.16	−0.03-0.03			
LWCC	a_{CDOM}	0.0129	0.0028	0.0037	2.0	2.5	15.2
10 cm cuvette in spectrophotometer	a_{CDOM}	0.0141	0.0187	0.0202	2.4	16.9	87.9
ICAM	a_{CDOM}	0.1013	0.0706	0.0310	45.1	114.5	125.8

by redirecting the source beam away from the detector, or indirectly by increasing the optical pathlength over the geometric pathlength. In an attempt to understand the relative accuracies for the different absorption measurement methods, we looked at the agreement between each method and the PSICAM spectrally and for each station (Fig. 19). Both RMSD and $\%\delta_{abs}$ deviations were found to be strongly wavelength dependent. RMSDs in comparison to PSICAM were higher at shorter wavelengths, consistent with spectral Type A uncertainty and CI relationships (Fig. 18). Conversely, spectral percent differences $\%\delta_{abs}$ were typically lowest at blue wavelengths where absorption was highest. An assessment of baseline uncertainties for different methods (see below) shows both properties are highly dependent on the strength of the absorption signal relative to effective pathlength, which explains some of the wavelength dependency of other uncertainty measures (CI, RMSD, $\%\delta_{abs}$). Absolute and relative deviations between PSICAM and the different instruments are summarized for three different wavelengths, 440, 555, and 676 nm (Table 5). Bench top methods show generally better agreement (2–11.5% $\%\delta_{abs}$ at 440 nm) with PSICAM than in situ methods (10–17% at 440 nm), which can be attributed to time–space sampling mismatches to some extent. However, conditions were stable and water column generally well mixed and, as a result, bias due to sampling mismatch is therefore unlikely to account for all the differences. In situ methods generally demonstrate poorer agreement due to the physical constraints of in situ instrumentation and deployment (i.e., size, weight, power, robustness), the environmental impacts on sensors compared to stable and controlled benchtop instruments, as well as the unique measurement approaches compatible with real-time, submersible flow-through implementation. For example, the unique measurement approach of the AC device results in a very significant scattering error that can only be marginally accounted for with various state-of-the-art correction approaches (Fig. 8; Stockley et al. 2017). Another example is the Trios OSCAR, a submersible implementation of the PSICAM design that was considered for inclusion in this study; however, small diameter flow ports in and out of the integrating cavity did not readily allow complete degassing when submerged, so the sensor could not be included.

LWCC and PSICAM a_{CDOM} measurements showed best agreement (within 5% at wavelengths < 600 nm) of all comparisons, which is not surprising as the PSICAM reflectivity is calibrated against the LWCC, which may cancel out some systematic errors. At longer wavelengths, the deviation increased (Fig. 19, Table 5), reflecting challenges of measuring very low levels of CDOM absorption at these wavelengths. Susceptibility to residual effects of water salinity and temperature are apparent. LWCC and PSICAM a_{CDOM} were also both offset corrected, assuming zero absorption at 700 nm; any real absorption by CDOM at 700 nm would be an example of a systematic error common to both approaches. However, the effects of this correction are typically negligible for any single measurement, and if done on all the measures, the relative relationships hold. It makes a difference in the statistical assessment of means, which is not the focus of this work.

Even under the assumption that particle scattering from colloids and nanoparticles is no concern for measurements of a_{CDOM}, measurements can be susceptible to scattering by bubbles introduced when the sample is pumped through the filter at the instrument's inlet. The presence of bubbles can potentially be a source of systematic error for all a_{CDOM} methods, although in situ methods are particularly susceptible. In shallow waters, persistent bubbles can be a significant challenge for filtered in situ measurements and variable large offsets in absorption were observed in AC-9 and AC-s data at multiple stations. The agreement with PSICAM data was higher for a_{nw} than for a_{CDOM} for the pumped in situ instrument ICAMs (Fig. 5), supporting the assumption of potential issues with the filtration for a_{CDOM} and residual bubbles. Data collected with AC devices here was not included in analysis due to obvious bubble contamination. Moreover, all stations were very shallow which meant that the typical degassing protocol, involving lowering instruments to ~10 m depth, could not be followed. Natural degassing in warming surface waters can likewise contribute to bubble contamination.

Comparison of data from different instruments of the AC design showed average agreement within 0.055 m^{-1} (RMSD) and < 9% ($\%\delta_{abs}$), demonstrating stability and strong replicability when following current protocols for calibration and corrections; comparison of final corrected data with PSICAM nonetheless showed deviations > 20% $\%\delta_{abs}$ in some cases, with highest errors at longer wavelengths likely driven by residual scattering errors.

Consistent with previous studies, recent advances in scattering correction approaches (*see* Fig. 8 and Table 3) improved the level of agreement between AC-s and AC-9 with respect to PSICAM in these turbid waters, most importantly avoiding the zero NIR absorption assumption, which is clearly shown to not be zero in the ISFP measurements (Fig. 14). Even though phytoplankton generally exhibit very small absorption in the NIR, nonalgal particles do have significant absorption and subtracting the NIR reduces their contribution throughout the visible spectrum. This is a concern for ocean color algorithm work because virtually all of the data in global data bases such as NASA SeaBASS have either the proportional or flat (baseline) corrections applied, which, as shown previously (Stockley et al. 2017), exhibit consistently large errors at longer wavelengths due to the null absorption assumption in the NIR. Ideally, if spectrally resolved ancillary data is available, absorption data may be corrected with the iterative correction, either using additional backscattering (McKee et al. 2013) or VSF (Stockley et al. 2017) data. However, if these additional data are not available, the semiempirical correction (Röttgers et al. 2013) is recommended, which has consistently shown comparable results. The analysis here contributes to existing

evidence that this correction approach, which does not require any ancillary measurements, is remarkably suitable for a wide variety of water types while also being convenient with minimal error propagation. Importantly, this approach may also be applied to AC data in historical databases as long as the measured absorption in the NIR was reported. More work is, however, required to establish its performance in very clear waters.

Even though scattering corrections appear to perform relatively well considering the magnitude of the correction (> 50% of a_m in red is typical), significant residual errors (~20%) between instruments remain, which is below acceptable levels for ocean color algorithm work (Werdell et al. 2018). Some of these differences may be attributed to natural variability in the scattering phase function governing the scattering error, but residual errors have systematic spectral dependencies consistent with previous findings (Stockley et al. 2017), suggesting generally applicable improvements in the scattering error may still be possible. However, results also highlight the critical need for other solutions for in situ measurements that may start to approach the accuracy of the PSICAM.

Moreover, the magnitude of deviation between ICAM and PSICAM was slightly larger relative to the AC-s or AC-9. This was largely driven by the lack of agreement at red wavelengths (Fig. 19) where $\%\delta_{abs}$ increased to up to 56% compared to 12% and 18% for AC-9 and AC-s respectively. Laboratory experiments raised concerns about ICAM performance due to the absence of a chlorophyll peak at 676 nm (Supporting Information Fig. S2). This was presumably because of interference of Chl *a* fluorescence which manifests as dampened absorption due to excess red fluorescence photons reaching the detector. The cause of this issue could not be determined with certainty; however, experiments with other nonfluorescing absorbing material indicated linearity in that red channel. A challenge with the ICAM is the lack of a NIR channel at which phytoplankton have no contribution and at which nonalgal particle contributions can be estimated semiempirically or with paired ISFP observations. Laboratory experiments with nonabsorbing scattering beads clearly demonstrate the ICAM, despite having an integrating cavity, is still prone to scattering errors of the same magnitude as found in the AC-s (Supporting Information Fig. S1). This is very likely from a highly anisotropic light field in the cavity due to suboptimal implementation. Interestingly, the agreement between the two ICAMs improved slightly for the a_p comparison relative to a_{nw}, suggesting systematic errors, possibly related to calibration, may have canceled to some extent when a_{CDOM} was subtracted.

The Gershun method can be challenging to implement and absorption estimates are affected by a range of different sources of uncertainties, including possible issues with quality of cosine collector response, spherical diffuser performance, immersion factors, and wavelength calibration. Here, we used an "out-of-the-box" approach, relying on manufacturer's data which can lead to known data quality issues due to poor characterization of radiometers and instrument drift over time (Mekaoui and Zibordi 2013; Zibordi et al. 2017; Talone and Zibordi 2018). Spectral $\%\delta_{abs}$ exhibited features of pure water absorption at longer wavelengths pointing toward issues with depth assignment during processing or with the accuracy of manufacturer's immersion factor (Zibordi and Darecki 2006). Furthermore, the Gershun approach is photon-limited at red/-NIR wavelengths which will limit its ability to accurately resolve spectral features in this range beyond the first optical depth (a few cm for some stations in this study), even when measurements are taken with a high depth resolution. Based on the results of radiative transfer simulations, inelastic radiative effects (Raman scattering and fluorescence) could be ruled out as significant sources of uncertainty and were therefore unable to explain the extent of the NIR deviation in these shallow turbid waters.

The choice of pure water absorption coefficients and temperature and salinity correction coefficients for pure water absorption are other potential sources of error for the Gershun approach. For example, more recent studies (Lee et al. 2015; Mason et al. 2016) suggest lower values at the blue/UV end of the spectrum which might improve agreement with other absorption measurement techniques at these wavelengths.

It is also important to finely resolve any vertical gradients in hydrographic and optical properties to accurately determine spectral absorption features with the Gershun method. For example, the presence of even small temperature and salinity gradients could affect pure water absorption (Sullivan et al. 2006; Röttgers et al. 2014), so that pure water absorption effects in neighboring measurements do not match, making it difficult to apply appropriate corrections. Similarly, if phytoplankton absorption was increasing with depth, the effect on differential irradiance would be to dampen associated absorption effects.

Another source of uncertainty was potentially inaccurate depth readings associated with the irradiance measurements. In this study, this was due to offsets between the radiometer collectors and the depth sensor, but erroneous depth readings could also arise from CTD calibrations and the air pressure tare, ship movement, wave effects, and the motion of the instrument package with mounted radiometers (Zibordi et al. 2004). This is a critical source of potential error, especially for turbid waters where irradiance differences had to be resolved over relatively small ranges in depth. Moreover, surface waves and wave focusing of irradiance require averaging of all parameters for each sampling sequence over some finite depth range. These averages are likely not precisely representative of radiometric measurements made at that exact average depth under a quiescent surface (Zaneveld et al. 2005), which is the assumption here. Importantly, uncertainties associated with the Gershun approach have not received the rigorous attention to detail and characterization over the years that

other methods reported here have received. The Gershun method would appear to warrant such attention to refine protocols; Fig. 13 demonstrates potential accuracies, with $\%\delta_{abs}$ reduced from 23.3% to 5.9% and RMSD reduced from 0.129 to 0.039 m^{-1}, if issues in resolving depth can be addressed. Importantly, these potential accuracies are in most cases better than all other in situ approaches. Multiple simultaneous measurements of the full irradiance quartet at known relative distance could help overcome some of the positioning issues. Moreover, out of all the approaches considered here, the Gershun method is the only one not involving perturbations of samples while resolving absorption over larger sample volumes more consistent with above water radiometry approaches. The method is also firmly grounded in radiative transfer theory with probably the least number of inherent assumptions of any method considered.

Many studies have focused on improving the methodology and characterizing uncertainties associated with the filter pad technique. Numerous sources of uncertainties in filter pad-derived a_p have been identified including incomplete detection of light scattered by the sample deposited on a filter, filter-to-filter effects due to differences in filter pads, variations in filter wetness during the measurement, distribution of particles on the filter, sample handing, filtration, temporal instability and effects due to sample storage, incomplete retention of particles on a filter and pathlength amplification due to multiple scattering within the sample/filter matrix (Stramski 1990; Mitchell and Kiefer 1998; Roesler 1998; Sosik 1999; Lohrenz 2000). Many of these problems are greatly reduced owing to the placement of filters inside the integrating sphere (Röttgers and Gehnke 2012; Stramski et al. 2015; Roesler et al. 2018).

However, the combination of some or all these sources of uncertainties still results in unavoidable aggregated uncertainty associated, for example, with the sample-dependent effects of the pathlength amplification factor, the largest source of uncertainty. Even though the exact origin of differences in regression slopes between individual samples could not be determined, they could be explained by this possible systematic error from filter pad inconsistency. However, much of the uncertainty is reduced by using a center-mounted integrating sphere configuration compared to traditional transmission mode measurements (Röttgers and Gehnke 2012; Stramski et al. 2015; Roesler et al. 2018), and optimizing sample processing techniques to reduce errors associated with each processing and analysis step.

Despite the range in water types between stations, the variability between filter pad methods was remarkably small. ISFP 1 and ISFP 2 a_p data agreed with onsite QFT-ICAM data to a comparable degree ($\%\delta_{abs} < 5\%$), suggesting very strong consistency among the different filter pad approaches and negligible effects associated with freezing and storage of samples (likely due to the nature of the sample), as well as small systematic bias associated with the determination of reference (blank) spectra. In addition, the level of agreement between the two ISFP approaches was broadly comparable for a_{nap} and a_p, suggesting that pigment bleaching or extraction processes have little effect on the amplification factor. The agreement with PSICAM a_p was fairly constant across the visible range for both ISFP and QFT-ICAM, within 7% and 9% ($\%\delta_{abs}$), respectively (Fig. 19, Table 5).

Common sources of variability among methods

Each method has several idiosyncratic characteristics that introduce potential variability and disagreement. Below are common sources of variability considered for all methods employed.

In situ turbidity

Agreement between all methods and the PSICAM was also sample-dependent with highest variability across instruments observed at stations with highest c_{nw} (532 nm), ST01, ST02, ST03, ST04, and ST10 (Fig. 20). With the exception of ST02, these stations were dominated by mineral particles with highest relative contribution of a_p to a_{nw} and a_{nap} to a_p (both ≥70%) at 440 nm as well as highest SPM and POC concentrations (> 12 g m^{-3} and > 790 mg m^{-3}, respectively) and lowest POC : SPM (< 0.065 g : g) ratios. High uncertainties and high variability between methods can therefore likely be attributed to natural variability due to station locations close to the opening of the lagoon with an increased exchange of water masses. The increased deviation with increasing turbidity reveals issues with sensitivity and/or scattering correction of AC-s, AC-9, and ICAM instruments.

There was no clear association between agreement with PSICAM data and Chl *a* concentration. The Gershun method underestimated absorption of all other methods, resulting in higher $\%\delta_{abs}$ across the spectrum for most stations.

Sample handling

All absorption measurements suffer from inherent sources of error associated with sample collection and calibration, potentially resulting in systematic bias in absorption data. One example is the hydrodynamic perturbation of the sample. This is both true for in situ measurements where samples are pumped through the instruments as well as discrete sample collection with Niskin bottles followed by sample release. The Gershun method has an advantage over the other approaches because it minimized perturbation of the water column. In addition to perturbation issues, natural changes in water masses in space and time can limit the comparability of absorption data measured with different methods. This study attempted to minimize effects of sample inconsistency by keeping water for discrete sample approaches well mixed in a single container before distributing water for measurements. Moreover, filters for measurements with the ISFP and QFT-ICAM method were all prepared by the same operator using the same filtration rig. However, it is extremely difficult to control how particles are deposited onto filters, especially for

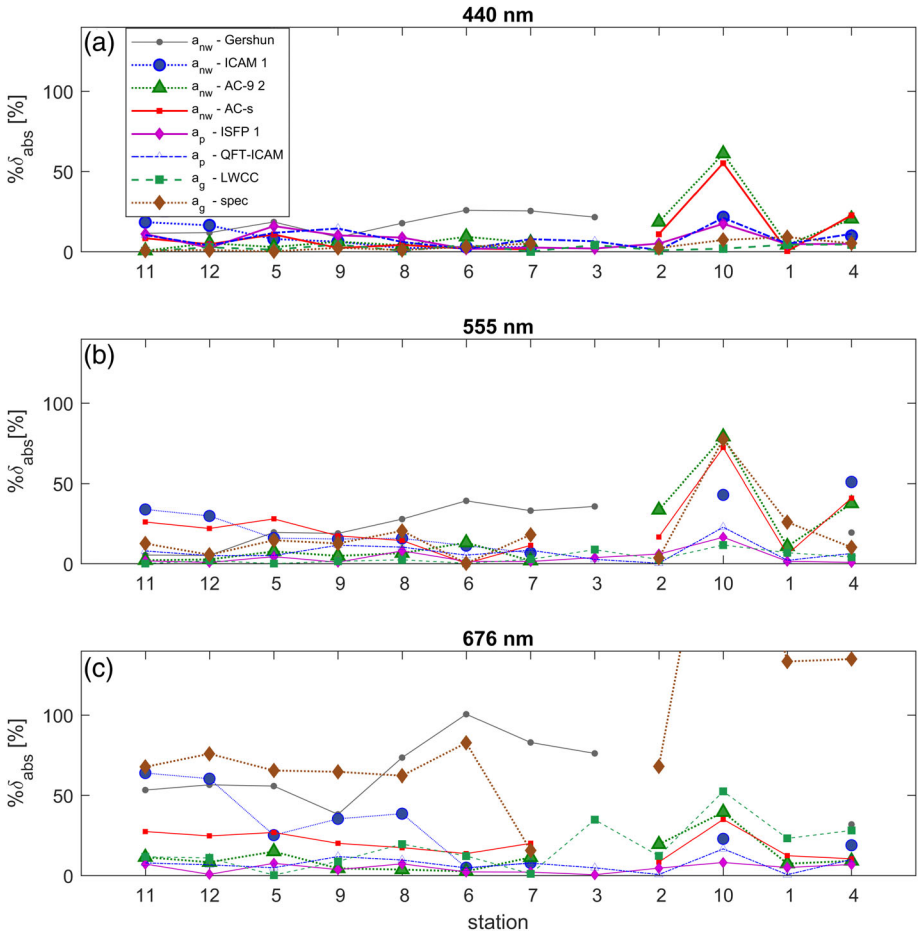

Fig 20. Variability in $\%\delta_{abs}$ at **(a)** 440 nm, **(b)** 555 nm and **(c)** 676 nm across different stations, sorted by nonwater turbidity (c_{nw} [532 nm]) with the least turbid station on the left and most turbid station on the right. While not the most turbid, Sta. 10 was the most variable with visible sediment plumes passing by in turbulent water. Different absorption parameters are compared to the PSICAM (LWCC: a_{CDOM}; ISFP & QFT-ICAM: a_p; AC-s, ICAM, Gershun: a_{nw}).

rare large particles, and potential for bias due to uneven particle distribution remains. Such differences are visible to the eye, and that provides additional information for contextualizing sample-to-sample variability. The location of the study provided slowly varying water properties over time. The average coefficient of variation in absorption at 488 nm, for example, was less than 2% over the sampling interval with the exception of Sta. 10, where it was 5% and visible sediment plumes flowed past the vessel in turbulent flow features. Variations of < 1% were observed over time scales of 5–10 min. Thus, even though in situ instruments were mounted on different frames, and water samples were collected at single time points within the in situ sampling interval, the variations observed between instruments is large compared to the in situ variability.

Sampled volume

Similarly, sample volumes differ across instruments. The largest volume sampled is associated with the Gershun approach because it is computed from discrete depth observations of water column light fields. Sample volume estimation is complex and depends on turbidity levels, maximum acquisition depth, depth resolution and arrangement of sensors on the frame. Determination of the exact sample volume was therefore not possible; however, it is estimated to be on the order of several m^3 for the water column associated with profiling depths (up to 4 m) in this study and, hence, many orders of magnitude larger than volumes associated with any other approach. The ICAM tube holds approximately 0.4 L and the illuminated volume within an AC-s tube is about 0.030 L. With an external pump drawing approximately 1 L/min through the sample tubes, independent realizations are collected approximately every 25 and 0.6 s, respectively. Discrete analysis volumes ranged from 0.05 (cuvette and some QFT-ICAM filters) to 0.4 L, comparable to the instantaneous sample volume of the AC-s, AC-9, and ICAM sensors, with the exception of the LWCC which only requires a few mL of sample volume. Thus, although the in situ sensors collected many

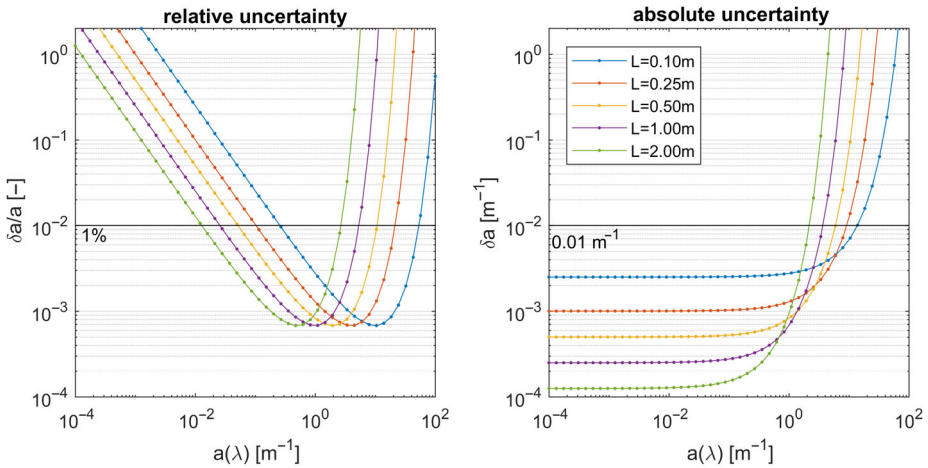

Fig 21. Estimated relative (left) and absolute baseline uncertainty (right) associated with instrumental noise as calculated in Eqs. 4 and 5, for different optical pathlengths between 0.1 and 2 m and an instrument noise $dT = 0.00025$, the approximate noise in transmission for AC devices. Note optimal relative uncertainty occurs at $a = 1/L$.

samples, each sample was of comparable volume to the discrete analyses. However, temporal averaging of time series data from these instruments increases effective sample volumes and lowers signal-to-noise. As a result, effects of small-scale patchiness and rare large particles may not be comparable between the various measurement approaches.

Instrumental noise

For every approach, there is a contribution to measurement variability due to inherent instrument noise which can be quantified by assessing the variability of absorption signals in a stable medium, such as purified water or air. Instrument noise typically varies with wavelength with largest uncertainties at the edges of the spectrum associated with lamp energy and/or detector stability. The mean standard deviation for repeated purified water measurements in a PSICAM is 0.0008 m^{-1} (Röttgers and Doerffer 2007) and < 0.001 m^{-1} in a LWCC. AC device noise levels are comparable except in very turbid waters (higher than observed here; Fig. 21). In dual-beam spectrophotometers, the magnitude of uncertainty depends on a combination of the instrument manufacturer's specifications for photometric accuracy, stability and noise, typically ranging from 0.002 to 0.01 m^{-1} for measurement with 10-cm cuvettes (IOCCG Protocol Series—Vol. 5.0, 2020). Average reference (blank) filter measurements for a_p determination with the ISFP method (ISFP 1) were within 0.0005 OD. The mean standard deviation for measurements in the QFT-ICAM was 0.0006 OD (Röttgers and Gehnke 2012).

For any absorption method with an instrumental noise of transmittance measurements dT, baseline uncertainties associated with instrument noise can be estimated using Eqs. 4 and 5. Figure 21 shows example calculations of baseline uncertainties associated with instrument noise, that is, the approximate relative and absolute uncertainty for different pathlengths, L, if the sample cell was filled with varying levels of absorbing material and no scatterers, assuming an instrument noise $dT = 0.00025$ (comparable to noise of transmission for AC devices). For example, for an AC-s with a 25-cm cuvette, the relative uncertainty associated with instrument noise computed using Eq. 4 is better than 1% for an absorption range of about 0.1–11 m^{-1}, while the absolute uncertainty as computed in Eq. 5 is lower than 0.01 m^{-1} for absorption values up to 9 m^{-1}. The geometric pathlength for the ISFP method is computed from the ratio of the volume filtered to the effective filter area. The pathlength range of 0.1–2.0 m represents filter volumes of approximately 50–750 mL for effective filter areas with approximate diameters of 2.2 cm, and spectrophotometers used in filter-pad measurements have comparable instrumental noise. The average pathlength of an integrating cavity is a complex function of cavity size, shape, and reflectivity, and the absorption of a sample (Kirk 1995). Since average pathlength is directly dependent on absorption magnitude, that is, pathlength decreases with increasing absorption, the relationships shown in Fig. 21 are not directly applicable. Similarly, estimation of the optical pathlength of filter pad measurements are also complex and the question whether this kind of analysis can provide guidance for optimizing filter volumes as a function of sample absorption requires more rigorous work.

These conceptual analyses provide guidance for determining optimal pathlengths to optimize an instrument's relative baseline uncertainty and minimize its absolute baseline uncertainty due to instrumental noise. Both types of baseline uncertainty continually change as a function of absorption magnitude and will therefore change with changing sample characteristics. An instrument's optimum relative uncertainty associated with instrument noise is at approximately $a = 1/L$ and the shape of the baseline uncertainty relationship relative to absorption is not dependent on instrument noise, dT,

which only shifts the relationship geometrically. These conceptual considerations of baseline uncertainty can be used to identify an optimal range of water absorption for a specific spectrophotometer configuration, which is almost entirely dependent on the specific instrument pathlength. Or in turn, one may use these baseline uncertainty relationships to choose the optimal pathlength, as possible within physical constraints of the instrument. This also generally applies to integrating sphere devices, where, for example, increasing cavity size will increase pathlength and accuracy for clear waters, although the relationships are more complex.

Propagated methodological uncertainty

The propagated uncertainty associated with each measurement is the square root of the sum of squared uncertainty associated with each methodological step and computation following Eq. 3. Given the filtered volume, filter clearance area and pathlength amplification correction, standard uncertainties of the absorption coefficients can be estimated, which were 0.008 m^{-1} for ISFP and 0.002 m^{-1} in the QFT-ICAM, with filtered volumes of 100 and 50 mL, respectively. Operational uncertainties, that is, after considering apparent systematic and random variability, for WET Labs AC instruments are typically 0.005 m^{-1} across all wavebands for particle-free water (after purified water calibrations). For the AC-s, variability can be higher in the blue due to weaker incident light intensity. Occasional deviations $> 0.005\ m^{-1}$ observed in previous comparisons with PSICAM have been attributed to time–space sample variability and possibly bubble contamination in the AC flow cell (Stockley et al. 2017). Baseline random noise for AC-9 devices is typically 0.001 m^{-1} and lower (Twardowski et al. 2018b; Fig. 21). Standard deviations of similar ICAM calibrations with purified water determined in this study were $< 0.002\ m^{-1}$ or 3% of pure water absorption coefficients. Comparable measurements for the Gershun method are not easily obtained and noise inherent to the approach is therefore not determined.

Examples of propagated uncertainty for filter pad absorption estimates of a_p and a_{nw} estimates from an AC-s are provided as an example pipeline for data processing (Supporting Information Appendix S1), with the caveat that not every source of uncertainty is identified, and some identified sources cannot be quantified. However, it is recommended that the approach to quantification should be used with details provided so that derived data products can be accurately compared in context, and future work in this area is required for all the methods included in this study.

In comparison to inherent instrument noise, 95% CIs (i.e., 1.96 × standard deviation of replicates or time series) provide estimates of a method's overall precision, stability, and replicability over time. CIs are aggregated errors reflecting a range of underlying sources of uncertainty, such as natural variability of the sample, lamp stability, consistency of the optical components, detector stability and internal error sources (nonlinearity, stray light), wavelength accuracy, operator consistency (sample handling and storage), temperature, salinity, the presence of bubbles and, where applicable, variability in particle distributions on filters.

Bulk uncertainty estimates based on CI or standard deviations, however, do not reflect systematic errors or provide information on the extent to which different uncertainty terms contribute to the overall estimate. Development of uncertainty equations for each method using mathematical error propagation, as described by Roesler et al. (2018) for the ISFP method, is desirable; however, it is not straightforward as quantification of all contributing uncertainty terms is required, which is not yet available for most methods and thus relies on identification of the order of uncertainty associated with each step.

In this study, we therefore focus on the quantification and comparison of CIs providing overall estimates of uncertainties associated with each method. With the exception of PSICAM and LWCC, that showed extremely high replicability, these bulk uncertainties were often significantly larger than the inherent noise of the method, often by an order of magnitude (driven by small scale patchiness for samples including particulate matter). It should be noted, that comparison of in situ approaches with discrete sample approaches is somewhat limited by fundamental differences in sample collection. In situ absorption spectra were derived from time series measurements and, hence, are representative of a much greater number of data points (> 10) than any of the replicate sample methods with typically six to nine different measurements included in an average absorption spectrum. Averaging on one hand reduces signal-to-noise, but also potentially introduces effects from environmental fluctuations over time from small-scale patchiness during the measurement. Time series averages also confound both natural variations and sensor uncertainty, although the former will dominate CIs in the presence of particles, while the uncertainty associated with discrete analyses is purely analytical. That said, the environment sampled in this study was demonstrably invariant at each station, resulting in relatively constant elevation of CIs. The differences between methods and CIs were driven by systematic variability.

Absorption is an exponential response derived from two measurements, incident and transmitted radiant power, these uncertainty concepts are not simply applied. The radiant power decreases exponentially with linear increase in absorbing material and thus the accuracy (uncertainty/magnitude) is proportional to e^{aL}/aL, where L is the geometric pathlength and reaches a peak when $a = L^{-1}$. This uncertainty is inherent Type A noise. Thus, accuracy is not only poor for low absorption coefficients, but also at high absorption coefficients where the uncertainty increases significantly as the transmitted radiant power becomes very small (Fig. 21). Most systematic errors are likewise not constant, but scale with absorption magnitude or some other factor that may or may not be related to absorption magnitude. So both types of uncertainty

will vary as a function of magnitude. This points to the importance of being cognizant of the environmental absorption range, so the operator can best characterize uncertainties within a range of interest. Assessing Type A instrument noise for spectrophotometers is straightforward, and by examining accuracy by the ratio above would be instructive as the baseline minimum uncertainty for any given pathlength. Then sources of systematic variability can be quantified within the appropriate ranges for the environment in question.

Recommendations

Results from this study have highlighted several limitations of current absorption approaches that will need to be addressed to improve the quality of hyperspectral absorption measurements in complex waters, either by closing remaining technological gaps or by improving state-of-the art methodologies for existing sensors:

Considering the strength of the absorption signal

Optical pathlengths should be chosen to optimize accuracy in water absorption ranges of interest. Flow cell pathlength options of 10 and 25 cm for commercial AC devices do not optimize accuracy in very turbid waters or the clearest ocean waters. The commercially available PSICAM has similar constraints due to the single 9-cm cavity size that is available. Röttgers et al. (2014) have shown a 5-cm cavity enables measurements of a_{nw} up to 20 m^{-1}.

For the filter pad technique, sensitivity can easily be tuned by adjusting filtration volumes, which affects pathlength.

Multispectral vs. hyperspectral methods

Future hyperspectral ocean color sensors such as PACE's Ocean Color Instrument (OCI) will require capabilities for validation of the absorption coefficients with 5-nm spectral resolution. While this suggests that only the hyperspectral instruments such as the AC-s and PSICAM will be useful, it is important to recall that (1) the multichannel AC-9 provides superior uncertainty and stability albeit at nine wavelengths, which could support improved multispectral validation merged with the hyperspectral coverage, (2) the ICAM currently provides robust assessment of UV absorption in situ albeit at one wavelength, (3) the hyperspectral AC-s provides spectrally smoothed output data which must be 'unsmoothed' to retrieve independent 5-nm resolution for hyperspectral validation (Chase et al. 2013). We note the AC-9 is no longer commercially available.

AC scattering correction

If spectrally resolved ancillary data are available, absorption data may be corrected with the iterative correction, either using additional backscattering (McKee et al. 2013) or VSF (Stockley et al. 2017) data. If no ancillary data are available, the semiempirical method (Röttgers et al. 2013) is the currently recommended AC scattering correction as it has consistently shown strong performance in a wide range of water types and also benefits from less error propagation. However, more assessment is needed in clearest ocean waters.

Improving ICAM measurements

The ICAM was found to significantly overestimate of absorption (of the same magnitude as uncorrected AC absorption) in these coastal waters, suggesting that measurements need to be corrected for scattering errors. The ICAM's spectral range should therefore be extended into the NIR to enable the application of existing scattering corrections. Furthermore, future work should focus on the development of a fluorescence correction for the ICAM to reduce potential fluorescence effects on absorption measurements in the red that we identified during laboratory experiments.

Exploiting the Gershun approach

The Gershun approach has strong potential because of the lack of sampling impacts, large effective sample volume, and the soundness of the underlying theory. The approach deserves more attention in addressing some of the challenges in implementation and working to refine and better account for potential sources of systematic variability, such as depth fluctuations. Augmenting existing radiometric profiling systems to include all measurements needed for the Gershun method should be considered and radiometers should be carefully characterized for drift, performance of the cosine collector, wavelength calibration, immersion factors and spherical diffuser performance. The E_{od} parameter is also being considered in emerging OC algorithms for PACE (Twardowski and Tonizzo 2018), so routine measurements may offer additional potential benefits.

New in situ sensors

Existing AC device and ICAM in situ absorption meters have significant scattering errors that cannot be corrected within uncertainties required for ocean color algorithm work. Even though commercial in situ instruments based on the ICAM design such as the HOBI Labs a-sphere and the TriOS OSCAR have been available (the a-sphere cannot currently be purchased), these lack the accuracy and sensitivity of the bench top set-up. Restricted flows through an integrating sphere assembly have been problematic in field deployments. We therefore emphasize the need for development of new in situ measurement devices with uncertainty and accuracy approaching the bench-top PSICAM, including instruments suitable for autonomous gliders and floats.

Routine measurements into the UV, possibly to 300 nm

Commercial in situ absorption meters with measurements extending into the UV range have not been developed to date. Although measurements in the UV can be made routinely with the bench top QFT, the tendency for some materials to bleach when exposed to UV light during measurements should be considered. Artifacts in measuring particulate absorption in the UV on filter pad range from challenges to accurately quantify UV-absorbing compounds to low signal-

to-noise ratio by filters that are strong absorbers of UV light. Thus, in situ absorption measurements of particle suspensions might be better suited in this spectral range. Certainly, the robust absorption measurements at the ICAM's 365-nm channel demonstrate the capability for extension to shorter wavelengths.

Uncertainty assessments and propagation

This study has demonstrated the importance of assessing the measurement uncertainties for any given method, considering both natural and instrumental variability. The examples of arithmetic propagation of uncertainties should be repeated for any new approach. This will require thorough characterization of all sources of uncertainty.

Absorption closure in clearest waters

The efforts presented in this study should be extended to the clearest waters to test uncertainty limitations with high importance for global ocean remote sensing and optical models.

References

Babin, M., D. Stramski, G. M. Ferrari, H. Claustre, A. Bricaud, G. Obolensky, and N. Hoepffner. 2003. Variations in the light absorption coefficients of phytoplankton, non-algal particles, and dissolved organic matter in coastal waters around Europe. J. Geophys. Res. **108**: 3211. doi:10.1029/2001JC000882

Babin, M., and D. Stramski. 2004. Variations in the mass-specific absorption coefficient of mineral particles suspended in water. Limnol. Oceanogr. **49**: 756–767. doi:10.4319/lo.2004.49.3.0756

Behrenfeld, M. J., and P. G. Falkowski. 1997. A consumer's guide to phytoplankton primary productivity models. Limnol. Oceanogr. **42**: 1479–1491.

Bowers, D. G., and C. E. Binding. 2006. The optical properties of mineral suspended particles: A review and synthesis. Estuar. Coast. Shelf Sci. **67**(1-2): 219–230. doi:10.1016/j.ecss.2005.11.010

Bricaud, A., A. Morel, and L. Prieur. 1981. Absorption by dissolved organic matter of the sea (yellow substance) in the UV and visible domains. Limnol. Oceanogr. **26**: 43–53.

Bricaud, A., and D. Stramski. 1990. Spectral absorption coefficients of living phytoplankton and non-algal biogenous matter: A comparison between the Peru upwelling area and Sargasso Sea. Limnol. Oceanogr. **35**: 562–582.

Chase, A., E. Boss, R. Zaneveld, A. Bricaud, H. Claustre, J. Ras, G. Dall'Olmo, and T. K. Westberry. 2013. Decomposition of in situ particulate absorption spectra. Meth. Oceanogr. **7**: 110–124. doi:10.1016/j.mio.2014.02.002

Del Castillo, C., Platnick, S., Antoine, D., Balch, B., Behrenfeld, M., Boss, E., Cairns, B., Chowdhary, J., DaSilva, A., Diner, D., Dubovik, O., Franz, B., Frouin, R., Gregg, W., Huemmrich, K. F., Kahn, R., Marshak, A., Massie, S., McClain, C., McNaughton, C., Meister, G., Mitchell, G., Muller-Karger, F., Puschell, J., Riedi, J., Siegel, D., Wang, M., Werdell, J., Del Castillo, C. E. (ed). (2012). PACE mission science definition team report. NASA. Available from https://pace.oceansciences.org/docs/pace_sdt_report_final.pdf

Ferrari, G. M., and S. Tassan. 1999. A method using chemical oxidation to remove light absorption by phytoplankton pigments. J. Phycol. **35**: 1090–1098.

Floge, S. A., K. R. Hardy, E. Boss, and M. L. Wells. 2009. Analytical intercomparison between type I and type II long-pathlength liquid core waveguides for the measurement of chromophoric dissolved organic matter. Limnol. Oceanogr. Methods: 7. doi:10.4319/lom.2009.7.260

Fry, E. S., G. W. Kattawar, and R. M. Pope. 1992. Integrating cavity absorption meter. Appl. Optics **31**: 2055–2065.

Fry, E. S. 2018. Chapter 3: Integrating cavity absorption meters. *In* A. R. Neeley and A. Mannino [eds.], IOCCG Ocean Optics and Biogeochemistry Protocols for Satellite Ocean Colour Sensor Validation, v. **1.0**. NS, Canada: IOCCG, Dartmouth. doi:10.25607/OBP-119

Gershun, A. 1939. The light field. J. Math. Phys. **18**: 51–151.

Graff, J. R., T. K. Westberry, A. J. Milligan, M. B. Brown, G. Dall'Olmo, V. van van Dongen-Vogels, K. M. Reifel, and M. J. Behrenfeld. 2015. Analytical phytoplankton carbon measurements spanning diverse cosystems. Deep-Sea Res. Part I **102**: 16–25. doi:10.1016/j.dsr.2015.04.006

Gray, D. J., G. W. Kattawar, and E. S. Fry. 2006. Design and analysis of a flow-through integrating cavity absorption meter. Appl. Optics **45**: 8990–8998.

Højerslev, N. K. 1975. A spectral light absorption meter for measurements in the sea. Limnol. Oceanogr. **20**: 1024–1034.

Højerslev, N. K. 1994. A history of early optical oceanographic instrument design in Scandinavia, p. 118–147. *In* R. W. Spinrad, K. L. Carder, and M. J. Perry [eds.], Ocean Optics, chap. 7. New York: Oxford Univ. Press. doi:10.1093/oso/9780195068436.003.0011

Intergovernmental Oceanographic Commission. 1994. Protocols for the Joint Global Ocean Flux Study (JGOFS) Core Measurements. Paris, France, UNESCO-IOC, 170pp. *In* Knap, A., Michaels, A., Close, A., Ducklow, H., Dickson, A. [Eds], (Intergovernmental Oceanographic Commission Manuals and Guides: 29), (JGOFS Report; 19). Available from http://hdl.handle.net/11329/220

IOCCG Protocol Series. 2018. Inherent optical property measurements and protocols: Absorption coefficient. Boss, E., D'Sa, E.J., Freeman, S., Fry, E., Mueller, J.M., Pegau, S., Reynolds, R.A., Roesler, C., Röttgers, R., Stramski, D., Twardowski, M., and Zaneveld, J.R.V. Neeley, A. R. and Mannino, A. [eds.], IOCCG ocean optics and biogeochemistry protocols for Satellite Ocean colour sensor validation, V. **1.0**. IOCCG, Dartmouth, NS, Canada. doi:10.25607/OBP-119

IOCCG Protocol Series. 2019a. Beam transmission and attenuation coefficients: Instruments, characterization, field measurements and data analysis protocols. Boss, E., Twardowski, M., McKee, D., Cetinić, I. and Slade, W. In Neeley, A. R. and Cetinić I. [eds.], IOCCG Ocean optics and biogeochemistry protocols for Satellite Ocean colour sensor validation, V. **2.0**, IOCCG, Dartmouth, NS, Canada. doi:10.25607/OBP-458

IOCCG Protocol Series. 2019b. Inherent optical property measurements and protocols: Best practices for the collection and processing of ship-based underway flow-through optical data. Boss, E., Haëntjens, N., Ackleson, S.G., Balch, B., Chase, A., Dall'Olmo, G., Freeman, S., Liu, Y., Loftin, J., Neary, W., Nelson, N., Novak, M., Slade, W., Proctor, C., Tortell, P., and Westberry, T. In Neeley, A. R. and Mannino, A. [eds.], IOCCG ocean optics and biogeochemistry protocols for Satellite Ocean colour sensor validation, V. **4.0**. IOCCG, Dartmouth, NS, Canada. doi:10.25607/OBP-664

IOCCG Protocol Series. 2020. Measurement protocol of absorption by chromophoric dissolved organic matter (CDOM) and other dissolved materials (DRAFT). Mannino A., Novak M.G., Nelson N.B., Belz M., Berthon J.-F., Blough N. V., Boss E., Bricaud A., ChavesJ., Del Castillo C., Del Vecchio R., D'Sa E. J., Freeman S., Matsuoka A., Miller R. L., Neeley A. R., Röttgers R., Tzortziou M., and Werdell P. J. In Mannino, A. and Novak, M. G. [eds.], IOCCG ocean optics and biogeochemistry protocols for satellite ocean colour sensor validation, V. **5.0**. IOCCG, Dartmouth, NS, Canada. Available from https://ioccg.org/wp-content/uploads/2019/10/cdom_abs_protocol_public_draft-19oct-2019-sm.pdf

Jerlov, N. G. 1976. Marine Optics, 231 pp. Amsterdam, The Netherlands: Elsevier.

Joint Committee for Guides in Metrology. 2008. Evaluation of measurement data — Guide to the expression of uncertainty in measurement, GUM 1995 with minor corrections.

Kirk, J. T. O. 1995. Modeling the performance of an integrating-cavity absorption meter: Theory and calculations for a spherical cavity. Appl. Optics **34**: 4397–4408.

Kishino, M., M. Takahashi, N. Okami, and S. Ichimura. 1985. Estimation of the spectral absorption coefficients of phytoplankton in the sea. Bull. Mar. Sci. **37**: 634–642.

Lee, Z., K. L. Carder, and R. A. Arnone. 2002. Deriving inherent optical properties from water color: A multiband quasi-analytical algorithm for optically deep waters. Appl. Optics **41**: 5755–5772.

Lee, Z. P., J. Wei, K. Voss, M. Lewis, A. Bricaud, and Y. Huot. 2015. Hyperspectral absorption coefficient of "pure" seawater in the range of 350–550nm inverted from remote sensing reflectance. Appl. Optics **54**: 546–558. doi:10.1364/AO.54.000546

Lefering, I. 2012. Stray light and non-linearity characterization of different photo-diode array spectrometers. BSc Thesis. Hochschule Bremerhaven, Germany.

Lefering, I., R. Röttgers, R. Weeks, D. Connor, C. Utschig, K. Heymann, and D. McKee. 2016. Improved determination of particulate absorption from combined filter pad and PSICAM measurements. Opt. Express **24**: 24805–24823.

Lefering, I., R. Röttgers, C. Utschig, and D. McKee. 2017. Uncertainty budgets for liquid waveguide CDOM absorption measurements. Appl. Optics **56**: 6357–6366.

Lefering, I., R. Röttgers, C. Utschig, M. S. Twardowski, and D. McKee. 2018. Measurement uncertainties in PSICAM and reflective tube absorption meters. Opt. Express **26**: 24384–24402.

Lewis, M.R., Carr, M.E.; Feldman, G.C., Esaias,W. and C. McClain. 1990. Influence of penetrating solar-radiation on the heat-budget of the equatorial Pacific Ocean. Nature **347**: 543–545. doi:10.1038/347543a0

Li, L., D. Stramski, and M. Darecki. 2018. Characterization of the light field and apparent optical properties in the ocean euphotic layer based on hyperspectral measurements of irradiance quartet. Appl. Sci. **8**: 2677. doi:10.3390/app8122677

Loisel, H., D. Stramski, D. Dessailly, C. Jamet, L. Li, and R. A. Reynolds. 2018. An inverse model for estimating the optical absorption and backscattering coefficients of seawater from remote-sensing reflectance over a broad range of oceanic and coastal marine environments. J. Geophys. Res. Oceans **123**: 2141–2171. doi:10.1002/2017JC013632

Lohrenz, S. E. 2000. A novel theoretical approach to correct for pathlength amplification and variable sampling loading in measurements of particulate spectral absorption by quantitative filter technique. J. Plankton Res. **22**: 639–657. doi:10.1093/plankt/22.4.639

Maske, H., and H. Haardt. 1987. Quantitative in vivo absorption spectra of phytoplankton: Detrital absorption and comparison with fluorescence excitation spectra. Limnol. Oceanogr. **32**: 620–633.

Mason, J. D., M. T. Cone, and E. S. Fry. 2016. Ultraviolet (250–550nm) absorption spectrum of pure water. Appl. Optics **55**(25): 7163–7172. doi:10.1364/AO.55.007163

Mekaoui, S., and G. Zibordi. 2013. Cosine error for a class of hyperspectral irradiance sensors. Metrologia **50**(3): 187. doi:10.1088/0026-1394/50/3/187

McKee, D., J. Piskozub, R. Röttgers, and R. A. Reynolds. 2013. Evaluation and improvement of an iterative scattering correction scheme for in situ absorption and attenuation measurements. J. Atmos. Oceanic Tech. **30**: 1527–1541. doi:10.1175/JTECH-D-12-00150.1

Mitchell, B. G., and D. A. Kiefer. 1998. Chlorophyll-alpha specific absorption and fluorescence excitation-spectra for light-limited phytoplankton. Deep-Sea Res. **35**: 639–663. 10.1016/0198-0149(88)90024-6

Mobley, C. D. 1994. Light and water: Radiative transfer in natural waters. San Diego, CA: Academic Press.

Mobley, C. D. 1999. Estimation of the remote-sensing reflectance from above-surface measurements. Appl. Optics **38**: 7442–7455.

Morel, A., and L. Prieur. 1977. Analysis of variations in ocean color. Limnol. Ocean. **22**: 709–722. doi:10.4319/lo.1977.22.4.0709

Musser, J. A., E. S. Fry, and D. J. Gray. 2009. Flow-through integrating cavity absorption meter: Experimental results. Appl. Optics **48**: 3596–3602.

Organelli, E., C. Nuccio, L. Lazzara, J. Uitz, A. Bricaud, and L. Massi. 2017. On the discrimination of multiple phytoplankton groups from light absorption spectra of assemblages with mixed taxonomic composition and variable light conditions. Appl. Optics **56**: 3952–3968.

Parsons, T. R., Y. Maita, and C. M. Lalli. 1985. A manual of chemical and biological methods for seawater analysis. New York, NY: Elsevier. doi:10.1002/iroh.19850700634

Pegau, W. S., J. S. Cleveland, W. Doss, C. D. Kennedy, R. A. Maffione, J. L. Mueller, R. Stone, C. C. Trees, A. D. Weidemann, W. H. Wells, and J. R. V. Zaneveld. 1995. A comparison of methods for the measurement of the absorption coefficient in natural waters. J. Geophys. Res. **100**(C7): 13201–13220. doi:10.1029/95JC00456

Pope, R. M., and E. S. Fry. 1997. Absorption spectrum (380–700 nm) of pure water. II. Integrating cavity measurements. Appl. Opt. **36**: 8710–8723.

Roesler, C. S. 1998. Theoretical and experimental approaches to improve the accuracy of particulate absorption coefficients derived from the quantitative filter technique. Limnol. Oceanogr. **43**: 1649–1660.

Roesler, C. S., and M. J. Perry. 1995. In situ phytoplankton absorption, fluorescence emission, and particulate backscattering spectra determined from reflectance. J. Geophys. Res. **100**: 13279–13294. doi:10.1029/95JC00455

Roesler, C., D. Stramski, E. D'Sa, R. Röttgers, and R. A. Reynolds. 2018. Chapter 5: Spectrophotometric measurements of particulate absorption using filter pads. *In* A. R. Neeley and A. Mannino [eds.], IOCCG ocean optics and biogeochemistry protocols for satellite ocean colour sensor validation, v. **1.0**. Dartmouth, NS, Canada: IOCCG. doi:10.25607/OBP-119

Röttgers, R., 2018. Chapter 4: Point-source integrating cavity absorption meters. In Neeley, A. R. and Mannino, A. [eds.], IOCCG ocean optics and biogeochemistry protocols for satellite ocean colour sensor validation, V. **1.0**. IOCCG, Dartmouth, NS, Canada. doi:10.25607/OBP-119

Röttgers, R., W. Schönfeld, P. Kipp, and R. Doerffer. 2005. Practical test of a point-source integrating cavity absorption meter: The performance of different collector assemblies. Appl. Optics **44**: 5549–5560.

Röttgers, R., and R. Doerffer. 2007. Measurements of optical absorption by chromophoric dissolved organic matter using a point-source integrating-cavity absorption meter. Limnol. Oceanogr. Methods **5**: 126–135. doi:10.4319/lom.2007.5.126

Röttgers, R., and S. Gehnke. 2012. Measurement of light absorption by aquatic particles: Improvement of the quantitative filter technique by use of an integrating sphere approach. Appl. Optics **51**: 1336–1351. doi:10.1364/AO.51.001336

Röttgers, R., D. McKee, and S. B. Woźniak. 2013. Evaluation of scatter corrections for ac-9 absorption measurements in coastal waters. Methods Oceanogr. **7**: 21–39. doi:10.1016/j.mio.2013.11.001

Röttgers, R., C. Dupouy, B. B. Taylor, A. Bracher, and S. B. Woźniak. 2014. Mass-specific light absorption coefficients of natural aquatic particles in the near-infrared spectral region. Limnol. Oceanogr. **59**: 1449–1460. doi:10.4319/lo.2014.59.5.1449

Röttgers, R., D. Doxaran, and C. Dupouy. 2016. Quantitative filter technique measurements of spectral light absorption by aquatic particles using a portable integrating cavity absorption meter (QFT-ICAM). Opt. Express **24**: A1–A20.

Sathyendranath, S., V. Stuart, A. Nair, K. Oka, T. Nakane, H. Bouman, M.-H. Forget, H. Mass, and T. Platt. 2009. Carbon-to-chlorophyll ratio and growth rate of phytoplankton in the sea. Mar. Ecol. Prog. Ser. **383**: 73–84. doi:10.3354/meps07998

Sosik, H. M. 1999. Storage of marine particulate samples for light-absorption measurements. Limnol. Oceanogr. **44**: 1139–1141.

Stockley, N., R. Röttgers, D. McKee, I. Lefering, J. Sullivan, and M. Twardowski. 2017. Assessing uncertainties in scattering correction algorithms for reflective tube absorption measurements made with a WET Labs ac-9. Opt. Express **25**: A1139–A1153.

Stramski, D. 1990. Artifacts in measuring absorption spectra of phytoplankton collected on a filter. Limnol. Oceanogr. **35**: 1804–1809.

Stramski, D., and S. B. Woźniak. 2005. On the role of colloidal particles in light scattering in the ocean. Limnol. Oceanogr. **50**: 1581–1591. doi:10.4319/lo.2005.50.5.1581

Stramski, D., R. A. Reynolds, M. Babin, S. Kaczmarek, M. R. Lewis, R. Röttgers, A. Sciandra, M. Stramska, M. S. Twardowski, B. A. Franz, and H. Claustre. 2008. Relationships between the surface concentration of particulate organic carbon and optical properties in the eastern South Pacific and Eastern Atlantic Oceans. Biogeosciences **5**: 171–201.

Stramski, D., R. A. Reynolds, S. Kaczmarek, J. Uitz, and G. Zheng. 2015. Correction of pathlength amplification in the filter-pad technique for measurements of particulate absorption coefficient in the visible spectral region. Appl. Optics **54**: 6763–6782.

Sullivan, J. M., M. S. Twardowski, J. R. V. Zaneveld, C. M. Moore, A. H. Barnard, P. L. Donaghay, and B. Rhoades. 2006. Hyperspectral temperature and salt dependencies of absorption by water and heavy water in the 400–750 nm

spectral range. Appl. Optics **45**(21): 5294–5309. doi:10.1364/AO.45.005294

Talone, M., and G. Zibordi. 2018. Non-linear response of a class of hyperspectral radiometers. Metrologia **55**(5): 747–758. doi:10.1088/1681-7575/aadd7f

Tassan, S., and G. M. Ferrari. 1995. An alternative approach to absorption measurements of aquatic particles retained on filters. Limnol. Oceanogr. **40**: 1358–1368.

Tonizzo, A., M. Twardowski, S. McLean, K. Voss, M. Lewis, and C. Trees. 2017. Closure and uncertainty assessment for ocean color reflectance using measured volume scattering functions and reflective tube absorption coefficients with novel correction for scattering. Appl. Optics **56**(1): 130–146. doi:10.1364/AO.56.000130

Twardowski, M. S., J. M. Sullivan, P. L. Donaghay, and J. R. V. Zaneveld. 1999. Microscale quantification of the absorption by dissolved and particulate material in coastal waters with an ac-9. J. Atmos. Oceanic Tech. **16**(6): 691–707. https://doi.org/10.1175/1520-0426(1999)0160691:MQOTAB2.0.CO;2

Twardowski, M. S., E. Boss, J. M. Sullivan, and P. L. Donaghay. 2004. Modeling the spectral absorption by chromophoric dissolved organic matter. Mar. Chem. **89**(1-4): 69–88. doi:10.1016/j.marchem.2004.02.008

Twardowski, M. S., M. Lewis, A. Barnard, and J. R. V. Zaneveld. 2005. In-water instrumentation and platforms for ocean color remote sensing applications, p. 69–100. *In* R. L. Miller, C. E. Del Castillo, and B. A. McKee [eds.], Remote Sensing of Coastal Aquatic Waters. **7**. Dordrecht, The Netherlands: Springer Publishing. https://www.springer.com/gp/book/9781402030994#aboutBook

Twardowski, M.S., Röttgers, R. and D. Stramski. 2018a. Chapter 1: The absorption coefficient, an overview. In Neeley, A. R. and Mannino, A. [eds.], IOCCG ocean optics and biogeochemistry protocols for satellite ocean colour sensor validation, **V. 1.0**. IOCCG, Dartmouth, NS, Canada. doi:10.25607/OBP-119

Twardowski, M.S., Freeman, S., Pegau, S., Zaneveld, R.V., Mueller, J.L. and E. Boss. 2018b. Chapter 2: Reflective tube absorption meters. In Neeley, A. R. and Mannino, A. [eds.], IOCCG ocean optics and biogeochemistry protocols for satellite ocean colour sensor validation, V. **1.0**. IOCCG, Dartmouth, NS, Canada. doi:10.25607/OBP-119

Twardowski, M., and A. Tonizzo. 2018. Ocean color analytical model explicitly dependent on the volume scattering function. Appl. Sci., special issue on Ocean Optics (feature publication) **8**: 2684. doi:10.3390/app8122684

Twardowski, M., X. Zhang, S. Vagle, J. Sullivan, S. Freeman, H. Czerski, Y. You, L. Bi, and G. Kattawar. 2012. The optical volume scattering function in a surf zone inverted to derive sediment and bubble particle subpopulations. J. Geophys. Res. **117**(C00H17). doi:10.1029/2011JC007347

Tyler, J. E. 1960. An instrument for the measurement of the volume absorption coefficient of horizontally stratified water. UC San Diego: Library – Scripps Digital Collection. Retrieved from https://escholarship.org/uc/item/0jd3q4tw.

Tyler, J. E., W. H. Richardson & Holmes R. W. 1958. The optical properties of Lake Pend Oreille. U.S. Gov. Res. Rep., PB-153997, Contract Nobs-72092. SIO Reference: 58-80.

van der Linde, D. W. 1998. Protocol for determination of total suspended matter in oceans and coastal zones. Technical Note No. 1.98.182, CEC-JRC, Ispra, Italy.

Van Heukelem, L., and C. Thomas. 2005. The HPL method, Chap 5. In Hooker SB, et al [eds.], The second SeaWiFs HPLC analysis round robin experiment (SeaHARRE-2). NASA/TM-2005-212785, Washington, DC, p 88–89, Table 50. http://oceancolor.gsfc.nasa.gov/DOCS/SH2_TM2005_212785.pdf

Werdell, P. J., B. A. Franz, S. W. Bailey, G. C. Feldman, E. Boss, V. E. Brando, M. Dowell, T. Hirata, S. J. Lavender, Z. Lee, and H. Loisel. 2013. Generalized ocean color inversion model for retrieving marine inherent optical properties. Appl. Optics **52**: 2019–2037.

Werdell, P. J., L. I. McKinna, E. Boss, S. G. Ackleson, S. E. Craig, W. W. Gregg, Z. Lee, S. Maritorena, C. S. Roesler, C. S. Rousseaux, D. Stramski, J. M. Sullivan, M. S. Twardowski, M. Tzortziou, and X. Zhang. 2018. An overview of approaches and challenges for retrieving marine inherent optical properties from ocean color remote sensing. Prog. Oceanogr. **160**: 186–212. doi:10.1016/j.pocean.2018.01.001

Werdell, P. J., M. J. Behrenfeld, P. S. Bontempi, E. Boss, B. Cairns, G. T. Davis, B. A. Franz, U. B. Gliese, E. T. Gorman, O. Hasekamp, K. D. Knobelspiesse, A. Mannino, J. V. Martins, C. R. McClain, G. Meister, and L. Remer. 2019. The Plankton, Aerosol, Cloud, ocean Ecosystem (PACE) mission: Status, science, advances. Bull. Am. Meteorol. Soc. **100**: 1775–1794.

Woźniak, B., and J. Dera. 2007. Light absorption in sea water, 454 pp. Atmospheric and Oceanographic Sciences Library **33**. Springer.

Woźniak, S. B., D. Stramski, M. Stramska, R. A. Reynolds, V. M. Wright, E. Y. Miksic, M. Cichocka, and A. M. Cieplak. 2010. Optical variability of seawater in relation to particle concentration, composition, and size distribution in the nearshore marine environment at Imperial Beach. Calif. J. Geophys. Res. **115**: C08027. doi:10.1029/2009JC005554

Yentsch C. S. 1962. Measurement of visible light absorption by particulate matter in the ocean. Limnology and Oceanography. **7**: 207–217. Available from https://www.jstor.org/stable/2832917

Zaneveld, J. R. V., J. C. Kitchen, A. Bricaud, and C. Moore. 1992. Analysis of *in situ* spectral absorption meter data, p. 187–200. *In* G. D. Gilbert [ed.], Proceedings Ocean optics XI, v. **1750**. San Diego, CA: SPIE. doi:10.1117/12.140649

Zaneveld, J. R. V., J. C. Kitchen, and C. Moore. 1994. The scattering error correction of reflecting-tube absorption meters. Ocean Optics XII. Proc. SPIE **2258**: 44–55.

Zaneveld, J.R.V., C. Moore, A.H. Barnard, I. Walsh, M. S. Twardowski & G. C. Chang 2004. Correction and analysis of spectral absorption data taken with the WET Labs AC-S. Proceedings Ocean Optics XVII, Fremantle, Australia, 25–29 October 2004.

Zaneveld, J. R. V., A. Barnard, and E. Boss. 2005. Theoretical derivation of the depth average of remotely sensed optical parameters. Opt. Express **13**: 9052–9061.

Zhang, X. D., and D. J. Gray. 2015. Backscattering by very small particles in coastal waters. J. Geophys. Res. (Oceans) **120**(10): 6914–6926. doi:10.1002/2015JC010936

Zhang, X., L. Hu, Y. Xiong, Y. Huot, and D. Gray. 2020. Experimental estimates of optical backscattering associated with submicron particles in clear oceanic waters. Geophys. Res. Lett. **47**: e2020GL087100. https://doi.org/10.1029/2020GL087100

Zibordi, G., D. D'Alimonte, and J.-F. Berthon. 2004. An evaluation of depth resolution requirements for optical profiling in coastal waters. J. Atmos. Oceanic Tech. **21**(7): 1059–1073. doi:10.1175/1520-0426(2004)021<1059:AEODRR>2.0.CO;2

Zibordi, G., and M. Darecki. 2006. Immersion factors for the RAMSES series of hyper-spectral underwater radiometers. J. Opt. A Pure Appl. Opt. **8**: 252–258. doi:10.1088/1464-4258/8/3/005

Zibordi, G., M. Talone, and L. Jankowksi. 2017. Response to temperature of a class of *in situ* hyperspectral radiometers. J. Atmos. Oceanic Tech. **34**(8): 1795–1805. doi:10.1175/JTECH-D-17-0048.1

Acknowledgments

The authors would like to thank the captain and crew of the M/V Thunderforce. We acknowledge the tireless and precise field and lab support provided by Nicole Stockley, Chris Strait, and Malcolm McFarland and the unparalleled expertise of Jim Sullivan. Funding for this research was provided by the NASA Plankton Aerosol, Cloud ocean Ecosystem (PACE) Mission. Analysis and write up were supported by the Harbor Branch Oceanographic Institute Foundation. This project would not have been possible without Jeremy Werdell, PACE Science Chief and Paula Bontempi, Ocean Biology, and Biogeochemistry Program Manager. Lastly, we would like to thank two anonymous reviewers for their thorough and constructive review. Their substantial and encouraging feedback has helped to improve this manuscript and we greatly appreciate their contribution.

Submitted 14 September 2020
Revised 10 June 2021
Accepted 08 July 2021

Associate editor: Ivona Cetinic